Composing Chaos: An Experimental and Numerical Study of an Open Duct Mixing Flow

Guy Metcalfe, M. Rudman, A. Brydon, L. J. W. Graham, and R. Hamilton
CSIRO, Highett, Victoria 3190, Australia

DOI 10.1002/aic.10640

By using a programmed sequence of boundary motions to introduce flow reorientation to a steady, laminar axial flow in an open duct, we develop a novel device to investigate and exploit chaotic advection of viscously dominated (low Reynolds number) flows. The design and operation of the Rotated Arc Mixer (RAM) is discussed. Among other things, the RAM can effect good continuous mixing of viscous materials without use of any internal elements; moreover, the RAM has several control parameters to tune the chaotic advection, making it flexible for applications and theoretical developments. Numerical methods to discover the robust parameter regions where chaos covers the entire flow domain, and how these parameters change with fluid properties is also discussed. Poincaré sections, dye advection and residence time calculations are presented for Newtonian and non-Newtonian fluids. Experiments, including advection field, velocity field and residence-time measurements, confirm all aspects of the device for Newtonian fluids. *AIChE J,* 52: 9–28, 2006
Keywords: mixing, dispersion, viscous, non-Newtonian, chaos

Introduction

In blending materials it is often desirable to impart structure across multiple length scales of the finished product, whether anisotropic interleavings in composites or films, particle exfoliations in polymers, droplet distributions in emulsions, or complete homogenization upon mixing. Hill[1] has given several examples of structured products from the food and personal care industries. To produce commercial quantities of materials it is often advantageous to have a continuous blending process. When viscosity increases or length scale decreases sufficiently, energy considerations preclude mixing by turbulent flows, and blending may best be accomplished through chaotic advection. For continuous, laminar blending the question is how to practically and efficiently generate the chaotic advection in the flow which will impart the desired structure to the final product.

By chaotic advection we mean the (Lagrangian) motion of fluid (or other) particles in a deterministic (Eulerian) flow. Simple, repetitive changes to the geometry of the flow, such as periodic reorientation, can produce particle trajectories appearing wildly irregular. However, in reality these trajectories are not irregular: repetitive changes to the flow create a self-similar and self-refining action in the advection field. The generic picture of a chaotic advection field has interwoven regions of regular and chaotic motions. The regular regions are within the so-called KAM surfaces that are barriers to transport and appear as tubes in 3-Dimensional (3-D) flows. The chaotic regions are generally the well-mixed regions of fluid. Surfaces separating these interwoven regions are called manifolds and provide the organizing structure for transport and for all types of interactions in the fluid. A well-mixed system requires minimization of the regular regions to attain a globally chaotic state. Books by Ottino[2] and Wiggins[3] provide general background, definitions, and details. Associated with characterizing chaotic flows are many ideas from dynamical systems theory; Aref[4] gives an overview of nonlinear dynamical systems theory and its role in the development of chaotic advection in fluids.

In this article we develop a continuous, open duct flow to examine chaotic advection of viscously dominated (low Reyn-

---

Correspondence concerning this article should be addressed to G. Metcalfe at guy.metcalfe@csiro.au.
Current address of A. Brydon: Los Alamos National Laboratory, Box 1663, Los Alamos, NM 87545.

olds number) flows. For reasons that will become apparent we will call this flow the *Rotated Arc Mixer* (RAM) flow, of which a brief description has appeared elsewhere.[5] Among other things the RAM can effect good inline mixing of viscous materials without use of any internal elements, making its pressure drop for Newtonian fluids the same as that for an open pipe; moreover, the RAM has several control parameters to tune the chaotic advection, making it flexible in application. In addition, the RAM generates very low shear stress, and its flow is predominantly elongational. The RAM accomplishes these things by imposing a deterministic sequence of boundary motions tangential to the duct boundary on finite and distinct patches of the duct walls. The viscous stresses caused by these boundary motions produce concurrent deterministic reorientations in the steady, laminar flow. Horner et al.[6] have explored both tangential and normal boundary motions in 2-D to generate chaotic transport in open cavities, finding either effective at generating chaos in the flow.

There are two somewhat distinct inspirations for our investigations. On the one hand, there are industrial motives. Blending highly viscous fluids is a difficult problem in many applications, for example polymers, foods, and viscous fermentations. The required energy input is high and often precludes any recourse to turbulence. Dispersing some additives, particularly nanoparticles, into polymer matrices is an open problem.[7] Dissipation in agitated highly viscous fluids may overheat and damage material.[8] High shear rates, imparted by impellers or narrowly spaced baffles, may destroy or limit the yield in production of bioproducts.[9,10]

On the other hand, there are scientific curiosity motives. Only a handful of 3-D chaotic flows have been experimentally investigated. In 1995 Ottino et al.[11] gave a taxonomy of experimental chaotic flows, of which more than a dozen were 2-D but only three were 3-D: the partitioned pipe mixer, eccentric helical annular mixer,[12] and the twisted pipe mixer,[13] all of which are open flows. Since then only a few experimental flows, to our knowledge, have been added to the list: baffled cavity,[14] slowly stirred tanks,[15,16] and a 3-D extension[17] of the double-cylinder flow,[18] with only the last being an open flow. It is also interesting to note that while many of the above "academic" chaotic flows are caricatures of industrial flows—for example, the partitioned pipe of a Kenics static mixer, the double-cylinder of a twin-screw extruder—and take their inspiration from industry, very little so far that has been learned about chaotic advection seems to have been incorporated into general industry use.

Static mixers have been practical chaotic mixing devices—even perhaps without knowing it—since the 1960s, long before the concepts of chaotic fluid mixing became widespread in the 80s; they are widely used in industry. Streiff et al.[19] review industrial static mixer design. But, it was not until the 1980s that computers were powerful enough to allow computational models of static mixers,[20] and only recently have a few researchers applied dynamical systems ideas to the analysis of mixing mechanisms in and optimization of static mixers via computational models[21,22,23,24] and experiments.[25] However, while certainly practical mixing devices, from the point of view of generating chaotic mixing flows, static mixers are "brute force" mixers. Dense sets of physical baffles mechanically split and recombine the flows to generate the repeated stretching and folding needed for good mixing. However, the cost of generating chaos this way is high: the dense nests of baffles require a large pressure drop; and, the baffles may clog on fibers, particles, or on some rapidly reacting media.[26]

Another widely used blending device for viscous material is an extruder. The extrusion literature is vast and their designs many; even a brief review of the various benefits and drawbacks is far beyond the scope of this article. We merely note that the channels in screw extruders can be "unwound" mathematically and modeled as a duct flow driven by a moving boundary.[2] And it is here that chaotic advection ideas have been applied to enhance extruder performance.[27,28,29] We also note that extruders are generally high shear stress devices. However, studies of dispersion indicate that elongational stress disperses to smaller length scales;[30,31] moreover, Rauwendaal[32] has stressed the importance of elongational flow and reorientation of fluid elements as critical to enhancing performance, applying these ideas to single screw compounding extruders. When tuned to produce a globally chaotic state, the RAM flow is an almost purely elongational flow.

We also note recent work by Zumbrunnen and coworkers[17,33] who try to go beyond blending in extruder-like devices, and try to connect specific chaotic flow regimes to specific final material structures and properties. The interplay here between the chaotic flow and the interfacial tension, viscosity, rheology, reactivity—in general all of the properties—of the component materials is subtle (see for example Jana and coworkers,[34,35]) and only at the beginning of understanding—for example, we cannot specify in advance a target arrangement (other than the homogeneous arrangement) of components and then solve the inverse problem for the chaotic flow regime to realize the structure—but already material structures have been realized that can be created in no other way than by chaos. In this paper we will give experimental examples mainly for well-mixed states.

Traditionally low Reynolds number flows usually implied high viscosity. A relatively recent technological area of low Re flow is flow in microchannels, where the low Re is due to the small channel size (see for example Koch et al.[36]). At these length-scales moving parts are generally a poor design choice, so motionless duct flows are a natural candidate to manipulate microflows or for a micromixer. One approach to micromixing is to split the channel into finer and finer subchannels until length-scales are such that diffusion will rapidly homogenize within the subchannels, then to recombine the subchannels. Another approach is to scale down open duct designs, such as static mixers[37] or a twisted pipe mixer;[38] however, complex shapes are more expensive to mass produce, a crucial consideration for a microflow technology. While traditional duct mixer designs can be scaled down, microchannel size scales open up new ways to mix.[39,40,41] With modifications to the method of generating transverse flow presented in the design section the RAM also readily scales down for microflows while remaining tunable.

The unwound extruder channel, the static mixer, microchannels, and other continuous flow devices can be generically labeled *duct flows* and studied through a common mathematical framework,[2,42,43] particularly when the flow is restricted to be laminar. Like these others, the RAM flow is a continuous, open duct flow. Duct flows are 3-D flows such that the velocity field consists of a uniaxial flow, which marks out a special axial flow direction, and a 2-D flow transverse to the axial direction. Steady, laminar duct flows always give regular, nonchaotic

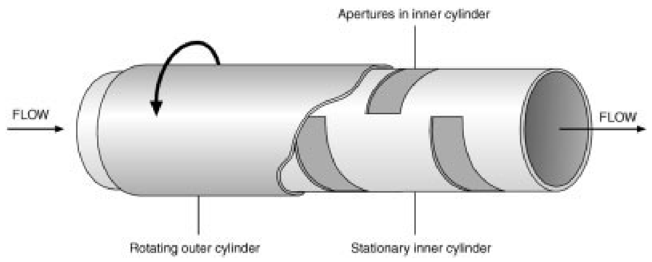

Figure 1. Rotated arc mixer.

An inner stationary cylinder with a sequence of apertures or windows cut through its wall and without internal structure is tightly wrapped by a concentric outer rotating cylinder. Liquids and additives flow axially through the inner cylinder where they are exposed to a sequence of transverse flows generated by the boundary motion at each aperture of the inner cylinder.

advection. However, if ways can be found to introduce *reorientation* to fluid elements as they pass along the duct, then the flow can generate chaotic advection.

The number of distinct chaotic advection fields that a given flow can produce is related to the size of the parameter space controlling the flow. A further issue is device flexibility. Parameters that can be tuned to keep desired optimum performance as throughput or material parameters change increase the range of a device's applicability. Most duct flows have a set configuration and are not tunable, the partitioned pipe mixer being one exception. For instance, when used as a heat exchanger[44] or micromixer[38] the twisted pipe mixer works optimally at one Reynolds number that depends on geometry: change the throughput rate and performance drops off. And static mixers have a complicated but fixed geometry that defines their advection characteristics regardless of any changes to input material properties. Tunability of the parameters determining the advection state are important for several reasons. We engage this point because the RAM has a large, tunable parameter space. This ability to adjust the flow from one chaotic state to another topologically distinct chaotic state is what we mean in this paper's title by *"composing chaos."*

Flow Geometry and Control Parameters

Neglecting diffusion, we expect no mixing in laminar flow through an open duct. However, consider what can happen if we can put selected areas of the duct boundary into motion. Because this kind of boundary motion generates no chaos, there is no advective mixing. What is missing is the ability of the flow to reorient the fluid particle paths after they undergo a certain amount of linear stretching. Flows discussed in the introduction can be chaotic and mix well precisely because they introduce fluid reorientation; all industrially useful continuous flow mixers reorient the fluid by introducing baffles and obstacles inside the duct. Here we describe a flow that uses sequences of boundary motions to reorient and efficiently mix or disperse in viscous liquids with no physical obstacle inside the duct. In this section we will describe the RAM flow's geometry and control parameters.

Geometry

Figure 1 shows the RAM flow. An inner cylinder is the duct through which will flow the liquids and other ingredients to be blended. The axial flow can be driven by any convenient means in any convenient orientation, so long as this inner duct remains full. Wrapped tightly around the inner cylinder is an outer cylinder. Selected surface elements of the inner cylinder wall are removed to leave apertures or *windows* through the inner cylinder wall. One or the other of the inner or outer cylinder is rotated—and for the mechanical realization in the present experiments we will restrict ourselves to an outer rotated cylinder. Wherever there are windows, the fluid in the inner cylinder will be in contact with the moving outer cylinder. Through viscous shear stress this boundary motion will drive a flow transverse to the axial flow. Seen in cross-section each window in the inner cylinder is an arc of boundary motion; each successive arc is rotated with respect to its predecessor; hence, the name, Rotated Arc Mixing flow.

As material moves down the RAM duct, it passes from the influence of the circulation field of one window of boundary motion to the influence of the next. Each subsequent boundary opening in the RAM is *offset* on the circumference of the stationary inner cylinder from its neighbors along the tube. The offsets provide the needed flow reorientation that is crucial to efficient generation of chaos. The amount of offset for the rotated arcs is a key parameter controlling the topology of the chaotic advection field.

Because the viscous drag from the rotating outer cylinder drives the transverse flow, the flow must be low Reynolds number in order for the transverse flow to penetrate significantly away from the window. As the Reynolds number rises, the transverse flow becomes confined to a thin region next to the moving boundary. Numerical simulations of the RAM for Newtonian fluids suggest that the mixing efficiency begins to degrade once the Reynolds number *Re* exceeds about 50. Once *Re* exceeds about 100, the RAM ceases to function as a robust mixer.

To the earlier general description of why and how the RAM works, we add two remarks on practical aspects of the RAM design based on rotating cylinders concerning (1) the thickness of the inner cylinder wall, and (2) the gap between inner and outer cylinders. The inner cylinder wall should be as thin as is compatible with structural stability. If too thick, instead of a moving boundary adjacent to the inner tube fluid, the boundary patch is across a cavity connected to the main flow. In practice we find that wall thicknesses of several percent of the inner diameter give no problems.

The gap between the inner and outer cylinders plays no role in the chaotic advection or mixing.

While fluid may—but due to high viscosity or surface tension may not—enter this gap, once fluid enters this gap it is "lost" to the analysis and control of mixing that we present. In practice we make this gap as small as is compatible with easy construction. There are larger gaps for some materials, such as plexiglas, that are difficult to precisely machine. For some applications, such as in foods or pharmaceuticals, clean in place requirements may disallow any gap at all. For these cases one would put seals around the windows or use sliding surface to surface contact with low coefficient of friction coatings to eliminate the gap altogether.

Control Parameters

In order for the transverse flows to extend from the moving boundaries over a significant portion of the domain, viscous

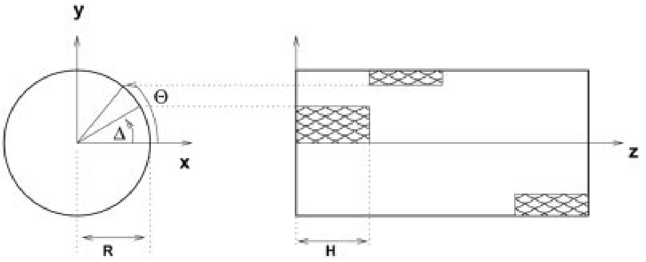

Figure 2. Geometric parameter definitions for the Rotated Arc Mixer.

R is the inner radius of the inner stationary cylinder; *H* is the window's axial length; and, Δ is the angle of the window opening. Θ is the angle by which each window is offset from its downstream neighbor.

stresses should predominate. This in turn implies operation at small Reynolds numbers. There are two Reynolds numbers for the RAM flow. $Re_{ax} = \bar{U}R/\nu$ and $Re_{cs} = V_R R/\nu$ are respectively the axial and cross-sectional Reynolds numbers, where $\bar{U}$ is the average axial velocity, $V_R = \Omega R$ is the boundary velocity with R the tube radius and Ω the outer cylinder rotation rate; ν is the kinematic viscosity. It is convenient to express these using the volume flux Q_v and to define Reynolds numbers experimentally as $Re_{ax} = Q_v/(\pi R\nu)$ and $Re_{cs} = \Omega R^2/\nu$.

Several parameters control the Lagrangian flow in the RAM, two geometrical and one kinematic. Figure 2 defines the geometrical parameters. The angular extent of a boundary window along the circumference of the inner tube is Δ. The offset around the circumference of successive boundary patches is Θ: the angular position of the start of any window is given by the angular position of the previous window plus Θ. Θ can be either positive or negative.

The kinematic parameter, which is adjustable during operation, is the ratio of rotational to axial velocities which, following the terminology of Kusch and Ottino,[12] we define as

$$\beta = \frac{\Omega R}{\bar{U}} \tag{1}$$

The kinematic interpretation of β is as the amount of transverse circulation or linear stretching within the interval between flow reorientations. The time between reorientations is the residence time in a window, $\tau_w \sim H/\bar{U}$, with H the axial length of a window (c.f. Figure 2). A typical circulation time is $\tau_c \sim \Omega^{-1}$. The ratio of reorientation interval to circulation time is $\tau_w/\tau_c \sim 2\Gamma_w\beta$ with $\Gamma_w = H/(2R)$ the window aspect ratio. As β increases, there is more transverse circulation or strain of the fluid within a reorientation interval. Whereas Δ and Θ are set once a RAM device is built, β is an adjustable parameter. This can be useful for changing the anisotrophy of blending or for adjusting to different rheologies.

It is convenient to also define

$$\beta_e \equiv \frac{\pi R^2 L\Omega}{NQ_v} = 2\Gamma\beta/N = 2\Gamma_w\beta \tag{2}$$

as an experimental parameter, where $\Gamma = L/D$ is the aspect ratio of a RAM tube of length L and diameter D, and N is the number of windows along the RAM tube. Using β_e has two advantages: (1) its components are directly and easily measurable without need for optical or physical access to the flow inside the duct; and (2) as β_e contains mixer volume over volume flow rate (defining the mean residence time t^*), it has a simple interpretation as $\beta_e = t^*\Omega/N$, mean residence time scaled by the rotation rate. An explicit connection between mixing kinematics and residence time can be useful when considering reactive flows. We will see that once β is chosen for a particular application to give a globally chaotic, well-mixed flow, then N will determine the final amount of striation refinement (c.f. Figure 16).

The control parameters for the RAM flow form the 3-D space (β, Θ, Δ), augmented by additional parameters describing the inertial, rheological, reactive or surface character of the materials prescribed for any particular application. All these parameters determine the advection field and, hence, the advection and mixing characteristics of the RAM. The design section presents methods for searching the control parameter space for mixing optima. Some regions of parameter space produce both globally efficient mixing and are parametrically robust in the sense that small, finite parameter changes do not severely degrade the mixing. However, first we will describe our computational and experimental methods.

Methods

To create, characterize, and control a duct flow capable of chaos, we require that, when superposed, the in-plane streamlines at one axial location should cross the streamlines from a downstream cross-section. This simplest of qualitative or intuitive methods to create chaotic flows has been alluded to in several articles.[18] Figure 3 explicitly illustrates the successive streamline crossings for the RAM flow. The lefthand column shows experimental photographs viewed from the inlet end of the mixing section of the duct. Flow is into the page. The shadows at 6 and 12 o'clock are dye injection ports. The righthand column shows streamlines of the analytical solution of Hwu et al.[45] of the 2-D Stokes flow matching the experiment. Figures 3a–d show the dye streak as it flows through the tube. In (a) the streak undergoes transverse rotation at the first window of boundary motion comparable to the analytical velocity solution. At a later time (b) the orientation of the streak's transverse motion has rotated; the orientation of the analytic solution has been rotated and superposed onto that of the original orientation. At later time (c) there is a further *reorientation* of the transverse velocity field. After this reorientation at later time (d) the dye streak has begun to loose it's regular structure. With flow through further reorientations the dye streak is stretched and folded into a globally chaotic advection.

Successive reorientation is a qualitatively sufficient method—well suited to thought experiments—to create chaotic flows. In the rest of this section we will describe our computational and experimental methods to quantitatively characterize, control, and optimize the RAM duct flow.

Computational

In order to explore and exploit both the structure in the 3-D RAM flow and its sensitivity to the control and material pa-

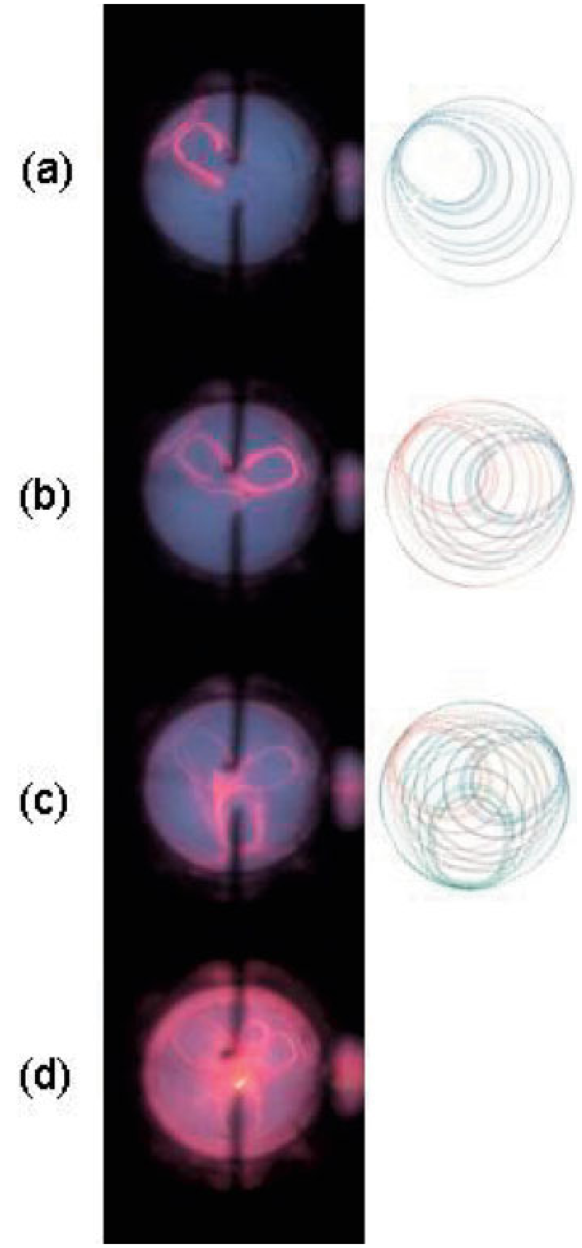

Figure 3. Superposed crossing of successive streamlines.

On the left are experiments injecting colored dye. The view is from the beginning of the mixing section; the vertical shadows are dye injection needles; and, the axial pipe flow is into the page. Photos a–d are taken at successive times from the start of dye injection. On the right are streamlines computed from the analytical crossflow solution.[45] To compare with the experiment, we have rotated the one solution and plotted them superposed. Panel d shows the emerging jumble of chaotic orbits.

rameters, we need to compute the advection field—how the entire collection of fluid elements evolves—as a function of this (large) space of parameters. With three kinematic parameters plus, however many material parameters we may need to incorporate, we will need to trade off between computation time and model exactness. While this tradeoff is hardly unique to our study, a 3+ dimensional parameter space is a very large space to explore, and ways must be found to make the search manageable. We have used four numerical models to study the RAM flow and advection, although the basic numerical procedure always has two steps: (1) Calculate the RAM flow field; and (2) Integrate fluid particle trajectories in this flow field to estimate the advection field. If the fluid elements have internal structure or interact with each other (through for example, surface tension, reactions, particles substantial enough to effect their local flow field, and so on), these effects can be incorporated, but as reported here will be neglected to focus on liquid advection alone. In each step alternative calculation methods give either a different level of approximation or different types of information.

Flow field calculation

The steady flow field in the RAM consists of two parts, the in-plane flow resulting from the moving arc boundaries and the axial flow that moves fluid along the duct. The velocity field can be written as

$$\mathbf{v} = \hat{z} \times \nabla\Psi + \hat{z}v_z \tag{3}$$

where Ψ is the in-plane stream-function, v_z is the axial flow, and $\hat{z}$ is the unit vector in the axial direction. These two parts may become nonlinearly coupled by the boundary conditions or material properties. How strongly Ψ and v_z couple determines whether separate fully 3-D numerical solutions are required for each point of parameter space, or whether reduced models with a significantly lower computational cost are applicable. Four models of increasing complexity have been used to calculate our flow field. They are

1. In-plane analytic solution, separable axial flow,
2. 2-D numerical solution, separable axial flow,
3. Two-and-a-half-D numerical solution, and
4. Fully 3-D numerical solution.

All of these methods are useful at different stages of this research.

In-plane Analytic Solution, Separable Axial Flow. In the Stokes limit of a Newtonian fluid, Hwu et al.[45] give an analytic solution for the stream-function in a circular domain driven by a nonzero tangential velocity along arbitrary multiple arcs of the domain boundary. If we assume **v** to be separable into decoupled in-plane and axial velocity fields, then the simplest option is to choose an analytical expression for v_z in Eq. 3. For instance choosing v_z to be Poiseuille (or a modified Poiseuille profile for some non-Newtonian fluids for which an analytic solution exists). Results predicted from pressure driven profiles are similar to those predicted from plug flow if the mean velocity replaces the peak velocity when calculating β. Because all flow fields in this approximation are analytic, the subsequent particle tracking is very efficient.

2-D Numerical Solution, Separable Axial Flow. If the cross-stream Reynolds number of the flow is higher than about 50 or if the fluid is non-Newtonian. Numerical solutions are determined using the commercial software CFX5.7, an unstructured mesh, finite volume code. In the simplest CFD approach, the in-plane analytic solution is replaced by the 2-D in-plane CFD solution, while still assuming an analytic axial flow profile. For integrating fluid particle motion velocity vectors must now be interpolated to particle positions in 2-D planes.

The interpolation uses the SRFPACK algorithms.[46] Note that coupling the analytic axial profile to the numerical profile in the case of non-Newtonian fluids is an approximation because the shear due to in-plane and axial flow will generally couple to modify both profiles, but in some circumstances it is a good approximation.

Two-and-a-Half-Dimensional Numerical Solution. A more accurate representation of non-Newtonian flows can be obtained by numerically solving an in-plane velocity field for all three components of velocity. We will call this a two-and-a-half-dimensional solution. It gives a good approximation to the flow field away from the ends of the appertures, and has been used in most of the calculations for non-Newtonian fluids. When using this solution, all three components of the velocity field must be interpolated to a fluid particle position, and the computational expense is approximately 50% higher than when using an analytic axial profile.

Fully 3-D Numerical Solution. For higher Reynolds numbers, inertial effects become important, and entrance and exit effects for each window begin to play a significant role in the flow field. Entrance and exit effects also play a role in some non-Newtonian fluids and in such cases, a fully 3-D flow field is required. This flow field must completely resolve each window and the transition from window to window. Thus, a typical computational geometry will involve simulation of many windows (often ten or more), resulting in necessarily large computational meshes and involve long run times to calculate the flow field. Interpolation of the velocity field to particle positions becomes a fully-3-D calculation, and computational times increase still further. This option is generally only used when confirmation of a design based on more approximate methods is desired.

An essential difference between the 3-D model and the "less than" 3-D models is the ability to use the 2- and 2.5-D models to build an overall cellular, periodic model of an N-window RAM flow. In essence the velocity field of the entire duct is assembled by "bolting together" reoriented copies of the solution within a single window. However, this introduces stress discontinuities at the cell boundaries that degrades the solution accuracy, particularly of the subsequently calculated advection. One way to make this obvious is to take the divergence of Eq. 3 evaluated at the $z = z_i$ window boundary. At the boundary $\mathbf{v} = [1 - H(z - z_i)]\mathbf{v}(i - 1) + H(z - z_i)\mathbf{v}(i)$, where $H(z)$ is the Heavyside function—$H(z = 0) = 1$ and $H(z \neq 0) = 0$—and $\mathbf{v}(i)$ denotes the velocity in the ith cell. The divergence is

$$\nabla \cdot \mathbf{v} = -\delta(z - z_i)v_z(i - 1) + \delta(z - z_i)v_z(i) \tag{4}$$

where we have used that the in-plane streamfunction is constructed to be divergence free in-plane. The divergence averaged over a cell is zero because the models conserve mass flow along the duct; however, at the boundary $\nabla \cdot \mathbf{v} = 0$ only if $v_z(i - 1) = v_z(i)$, that is if the axial flow field does not vary at boundary crossings. This will hold true whenever the assumption of completely decoupled in-plane and axial flow is valid, or strictly only in the Stokes limit for Newtonian fluids. Nonetheless, these stress discontinuities do not appear to be a serious modeling drawback until fluids are highly non-Newtonian. This is not unexpected: the Jones et al.[47] model for a twisted-pipe mixer and the Kusch and Ottino[12] model for the partitioned pipe flow always have non-zero divergence at cell boundaries yet give excellent comparison to experiments with Newtonian fluids. (We are not aware of experiments or computations of these flows using non-Newtonian fluids.) Aside from numerical discontinuities there are, moreover, real transitional effects associated with higher Reynolds numbers due to "spinning up" fluid up- and down-stream of a window boundary. On the other hand, the effect of the changeover from one flow reorientation to the next would be negligible if the changeover is confined to a small enough axial length around the window boundary, where "small enough" is in relation to the length of a window. This changeover length depends on Re and the rheology of the fluid (particularly for viscoelastic fluids). We quantify the changeover length in a later section as a function of Re. For most of the experiments reported here this changeover length is small ($<0.1H$), and negligible effect on the dye advection is verified by the agreement between experiment and 2- or 2.5-D computation.

In spite of some shortcomings of the periodic modelling approach the computational savings from the less than fully 3-D numerical solutions are significant. These savings come from being able to calculate the flow in a RAM cell once and then reuse this solution. For a 3-D solution we must grid and solve the flow for an N-window RAM. Each change of geometric parameter means generating a new grid, and each change of geometric, kinematic, or material parameter means calculating a new flow solution. Neglecting any parameters other than the (β, Θ, Δ) parameter space, examining this $n \times n \times n$ grid of parameters would require $\mathbb{O}(n^2)$ griddings and $\mathbb{O}(n^3)$ solvings. If instead we can solve for the flow within the axial length of one window, this being one cell of an assumed periodic flow, then solutions for N-windows in all (β, Θ) planes can be obtained by solving for the flow field once. During advection integration then, all velocity field data is obtained by rescaling and rotating the one solution. While the integration burden is unchanged, this reduces the flow field computation from an $\mathbb{O}(n^3)$ to $\mathbb{O}(n)$ burden. While assuming an axial periodic symmetry for the RAM flow is not required (for example, Θ could be made a random variable), being able to exploit this symmetry is well worth the loss of generality and the introduction of mild stress discontinuities between cells. However, it is worth keeping in mind that as the Reynolds number or "amount" of non-Newtonian behavior grows, cell transition effects in the velocity field will effect the advection field and fully 3-D simulations will be the only recourse. We have experimental evidence that viscoelastic fluids need fully 3-D simulations even for small (well below one) Deborah numbers.

Advection of fluid particle trajectories

The flow solution is used to integrate fluid particle trajectories to estimate the advection field. Our code is a variable step sixth-order Cash-Karp algorithm (from Numerical Recipes) with a time-stepping error tolerance of 10^{-7}, which was checked for adequacy. We will predominately use Poincaré sections and computational "dye" traces validated by subsequent experiments.

Poincaré sections plot the in-plane locations of a small number (10–20) of fluid particles every time they traverse one period of the axial flow, where a period is the length of duct for the window to return to its original orientation. Leaving aside that $\Theta/2\pi$ can be irrational and the orientation never exactly return, $\Theta/2\pi$ is typically greater than 10. In theory, this could strictly mean traversal of a great many appertures while building up enough periods for the section to show something. However, in practice points taken at the end of each aperture can be used, provided they are suitably rotated to maintain the moving arc in the same position. The Poincaré sections are built up over several thousand appertures and provide a clear picture of long-time advection behaviour in the RAM, revealing the geometry of the interlaced regions of chaos and regular islands (KAM torii). As Poincaré sections are computationally inexpensive, once they are computed for any selected dense grid of parameters, any areas of interest can be further examined with computationally more expensive methods.

While the Poincaré sections show the asymptotic structure for a given set of parameters, they provide no information on the rate at which this structure arises. Physically this is the rate at which fluid striations thin. In practice duct flows are of finite length—tens of appertures—and the short time and rate information is crucial for application designs. To get this short time and rate information, particularly about parameters for globally chaotic or fully mixing configurations, we use numerical dye traces. This generally consists of initially placing a large number of fluid particles (20 000–100 000) in a small region at the inlet of the RAM flow, then advecting these particles through the RAM and noting their spatial locations at the end of each apperture. A qualitative picture of striation distribution is then obtained by observing the particles as they are transported through the RAM. Alternatively, the particles could be distributed uniformly over an initial plane at the inlet, then released. If the particles' initial locations in the plane are tagged (say with colour), various statistics about their movement can be calculated. Discussion of methods to find optimized designs and of measures of well-mixed are presented later.

Experimental

Our experimental data consists of dye visualization images (digital and film) of the Lagrangian advection field, mixing measures and residence time distributions derived from the images, and laser Doppler velocimetry (LDV) measurements of the Eulerian velocity field. We report results from experiments on RAM devices of two sizes, large and small, made of clear acrylic.

The larger RAM has a stationary acrylic inner tube of inner radius $R = 44$ mm, length $L = 1{,}500$ mm, and thickness 3 mm. $N = 15$ windows are cut through the tube along the plan of Figure 1; determined by methods described later, $\Delta = \pi/4$ and $\Theta = +\pi/5$. The rotating outer acrylic tube fits concentrically and snugly around the inner with a gap of 0.8 mm, which is about 1% of the inner diameter. The tubes' diameters were chosen "off the shelf" to have as small a gap as possible because boring and polishing a 1.5 m length of acrylic is difficult. Too large a gap or too thick an inner cylinder would degrade the transmission of stress from the moving boundary to the interior of the fluid domain. Therefore some care should be taken to minimize these distances, while balancing ease of construction and structural stability. The ends of the RAM tubes were placed in sealed bearing blocks that also served to align and hold the inner tube. Rotating lip seals were used for the outer cylinder. Inlet and outlet pipes clamp onto the bearing blocks. This assembly was placed vertically and surrounded by a square tank that in operation was filled with glycerin to aid visualization and LDV measurements by refractive index matching to the outer curved acrylic tube.

The smaller RAM has $R = 18$ mm, $L = 600$ mm, and $N = 30$ with Δ and Θ as earlier. To make the gap between inner and outer cylinder small, the outer face of the inner cylinder was machined and polished. After cutting and polishing, the average inner cylinder thickness is 0.9 mm. The outer "cylinder" was made by drilling alignment bolt holes into a square bar of acrylic that was then cut in half lengthwise. After this a computer controlled mill machined and polished half cylinder surfaces into each half bar. These pieces were then bolted together to form an outer cylindrical surface, into which fitted the inner cylinder. This left a gap thickness of 0.15 mm, which is less than 0.5% of the inner cylinder diameter. The seals and bearing blocks of the smaller RAM are of similar design to those of the larger. The smaller RAM was operated horizontally. Right angle bends three diameters up- and down-stream of the RAM pipe section, allowed viewports for on-axis viewing and for photographing dye in laser-sheet illuminated planes.

To maintain constant volume flow rates for the larger, vertical experiment and for the smaller, horizontal experiment, we used different methods. For the vertical experiment we had a 200 Liter tank directly above the RAM section inlet. A pipe, six dia. long, led from the bottom of the tank past the dye injection ports to the inlet of the RAM section. This tank was fed by a pump and had an overflow weir to maintain a constant level. The volume flow rate was controlled by a valve 4 diameters, from the RAM section outlet. Exiting fluid could be discarded or recirculated. For the horizontal experiment we had a positive displacement pump (variable speed controlled Mono pump) between a reservoir tank and the RAM section inlet.

Two dye injectors are located one diameter upstream from the inlet of the RAM section. The shadows in Figure 3 show the injectors approximate radial location. The injectors are stainless steel needles whose cross-sectional areas are each 2% of the cross-sectional area of the RAM tube. Each needle is inserted radially through the pipe leading to the RAM inlet and bent 90° so that discharge is along the axial flow direction. Additionally each needle can be rotated, and its radial position changed so that dye can be injected at almost any point in the initial condition plane. In the larger device weight driven pistons injected dye; in the smaller device syringe pumps injected the dye.

The motor for outer cylinder rotation is variable speed controlled, and is connected by a timing belt to a gear collar attached to the outer cylinder adjacent to the upstream bearing block. Peripheral to the RAM tube section are standard tanks, pipes, valves, and pumps, on which there is no need to elaborate.

The working fluid is most commonly a 90% glycerol-water mixture of viscosity 1.50 Pa-s, measured by rheometer, and density 1.23 kg/m^3, from standard tables. Dyed fluid is made from the working fluid by mixing green or red rhodamine dye powder (Cole-Palmer), which floureses under ultra-violet light. A dense dye-laden fluid is first made. This is then diluted with working fluid until sufficiently density matched that a dye blob in a beaker of working fluid does not noticeably move over 60 min. As experimental mean residence times range from under a minute to almost 30 min, the expected diffusion distance after 30 min for a diffusion coefficient $D \sim 10^{-6}$ cm^2/sec is $\sqrt{Dt} \sim 10^{-2}$ cm. For these experiments we expect diffusion to play a negligible role.

The experimental procedure is straight forward. Prior to beginning an experiment, the working fluid was poured into the reservoir and circulated through the RAM section in a closed loop to thermally equilibrate the fluid and equipment, and to facilitate air bubbles leaving the fluid. A small amount of dye may be pushed through the dye injectors at this point to remove air from the dye lines, and the injectors are placed in their desired initial position. The targeted flow rate Q_v and rotation rate Ω are set and measured. To illuminate dye throughout the entire RAM length, we turn on UV lights placed on opposite sides of the RAM section. Then the syringe pump driving the dye injection is turned on. As the dye stream moves down the RAM section, stretching and folding, videos are taken. When the Reynold's numbers are small—and when not using elastic fluids—we can simultaneously stop the axial flow and rotation to freeze the dye stream to take deeply saturated still photos without effecting the motion of dyed fluid elements. Photos were taken on film or on a digital camera with 1024 × 1024 pixels.

The range and experimental uncertainly of the kinematic parameter β_e is derived from the uncertainties in measuring the flow rate and rotation rate; we take the geometrical factors in the definition of β_e as known exactly. The flow rates could range over $Q_v \in [1.5 \times 10^{-5}, 1.5 \times 10^{-7}]$ m^3/s. Q_v was measured with a stopwatch to collect a volume of fluid that was weighed and converted to volume using the table density of the working fluid. The largest contributor to measurement uncertainty were the hands operating the stopwatch and removing the beaker from the stream. But taking at least 2 min to collect kept the uncertainly in Q_v to below 1%. The rotation rates could range over $\Omega \in [0.3, 30]$ s^{-1}. The rotation rate was measured with a handheld tachometer to ±0.5 rpm, which at a typical rotation rate of 75 rpm gives a typical uncertainty in Ω of less than 1%. With these ranges of Q_v and Ω the adjustable kinematic parameter could range over $\beta_e \in [0.4, 400]$ though mainly we operated with $\beta_e \in [3, 30]$. The overall uncertainly in β_e was about ±1%. Both Re_{cs} and Re_{ax} are always below 10 in these experiments (except for checking higher Re effects) and have individual uncertainties about three quarters that of β_e.

For residence time distribution experiments we turn off the axial flow and rotation to position either a single large, stationary blob of dyed fluid in the center of the RAM inlet or distribute many smaller blobs over an initial plane at the inlet, then resume the axial flow and rotation. A digital camera records the dye intensity through an on-axis viewport as the dye stream passes through a 1 mm laser sheet oriented perpendicular to the axis and placed 2 mm after the end of the final window. As the smaller RAM has a square outer form, the camera was gated to the rotating tube's orientation, in order to always record with the same light distribution.

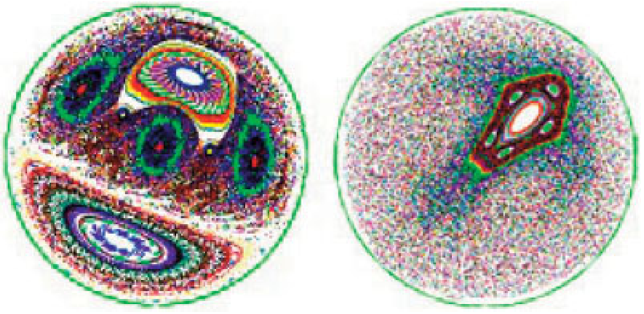

Figure 4. Example of effect of window opening size Δ on advection topology.

(Left) $\Delta = 135°$; (right) $\Delta = 90°$.

Design, Characterization, Mixing

There is only marginal advantage to having a large, tunable parameter space for chaotic advection without also having strategies to sift this space for desired regions of optimized functionality. Our strategy will be to use a variety of tools from dynamical systems theory to characterize chaotic advection. The spirit of this strategy, which follows Jana et al.,[18] is to use computationally cheap tools to coarsely "sieve" parameter space for a desired functionality, then to use ever more computationally expensive tools to refine selected regions of the coarse-grained parameter space toward an optimum. In this section, we describe this *dynamical sieve* and as an example of its use find a mixing optimum for Newtonian fluids. The good mixing is experimentally verified and further characterized by measuring its associated residence-time distribution.

Dynamical Sieve as Design Protocol

The control parameters for the RAM flow form the space (β, Θ, Δ), augmented for any particular application by additional parameters describing the fluids. In order to design a RAM for a given application, values for these three parameters should be determined numerically, as experimental parameter determination would be time-consuming. To streamline the following presentation, we will ignore variations of the parameter Δ and will consider only a window opening $\Delta = \pi/4$. This is not to say that Δ has no effect; on the contrary, for example Figure 4 shows Poincaré sections for two values of Δ in Stokes flow with other parameters equal. The effect of Δ can be large, but the procedure to sort through these effects is the same as described for the other parameters.

Jana et al.[18] give a computational cost ranking of dynamical systems diagnostics for chaotic advection. In order from least to most costly we have used Poincaré sections, dye traces and area coverage, and stretching distributions. It is worth noting that the stretching distributions are more than 10^3 times more costly than the other diagnostics, while a dye trace is only about a factor of ten more costly than a Poincaré section. Poincaré sections are constructed as described earlier. Regions of the section that form structures indicate transport barriers. Chaotic portions of the flow have a seemingly featureless jumble of points spread evenly over a region. Examples showing both regular and chaotic portions are in Figure 4.

Dye traces numerically mimic experiments where small amounts of dyed additive is either placed initially as a blob or continuously injected. The numerical dye lines are an initially dense collection of points (tens of thousands or more) that are advected and followed. As the points separate exponentially quickly over most of the line, it may be desirable to interpolate new points to maintain the integrity of the numerical dye. This exponential separation also means that it is impractical to follow the numerical dye interfaces for a large number of periods. However, after the Poincaré sections the object of the dye traces is to provide short to medium time information about the rate of structure development of the advection field, information Poincaré sections do not give. For instance, it can be that well-mixed states predicted by Poincaré section remain poorly mixed for hundreds of periods, leading to prediction of impractically large RAMs. The short time information from dye traces is crucial to proper design of a practical device based on chaotic advection. The area coverage of the flow is calculated from the final dye trace by projecting the dye line onto a plane perpendicular to the flow after the final window. The final cross-section of the pipe is divided into an $n \times n$ grid, where n is as close as possible to the square root of the number of particles in the computation. The area coverage is given by the fraction of squares which contain at least one particle. This is equivalent in an experiment to turning off the rotation and allowing whatever dye is in the RAM tube to flow out while recording the dye exit locations.

Stretching distributions can be used to refine parameter searches for well-mixed states. They can indicate local rates of mixing and how uniformly rates are distributed over the mixing region. On the other hand, interpretation of stretching distributions can be problematic, and they do not always discriminate very well between states. Moreover, it is extremely difficult to measure a stretching distribution, particularly for 3-D flows, in order to validate if computations are accurately capturing what happens in the flow. For this reason we have used stretching distributions sparingly.

An Example: Globally Well-Mixed

We now illustrate the dynamical sieve by finding the parameters to get a globally well-mixed flow for Newtonian fluids. The procedure is:

1. Calculate the flow field using an appropriate model as discussed earlier.

2. Track a small number of massless fluid particles in this flow field and determine Poincaré sections for a region of the (β, Θ) plane. Figure 5 shows such a plane of Poincaré sections. Flows that may potentially mix well have Poincaré sections in which the point density is evenly distributed across the entire cross section. Poincaré section from flows that will not mix well show one or more "islands," which impede mixing.

3. Identify regions in parameter space in which the Poincaré sections suggest good mixing and in which small changes to the parameters do not adversely effect the mixing. Examples are the boxed regions of Figure 5. This is necessary because isolated globally chaotic states can exist, but small changes to fluid or throughput parameters, such as will invariably happen in an industrial operation, will move the operating point into a neighboring, poorly mixed region of parameter space. Optimal regions of parameter space produce both globally efficient mixing and are parametrically robust in the sense that small parameter changes do not severely degrade the mixing.

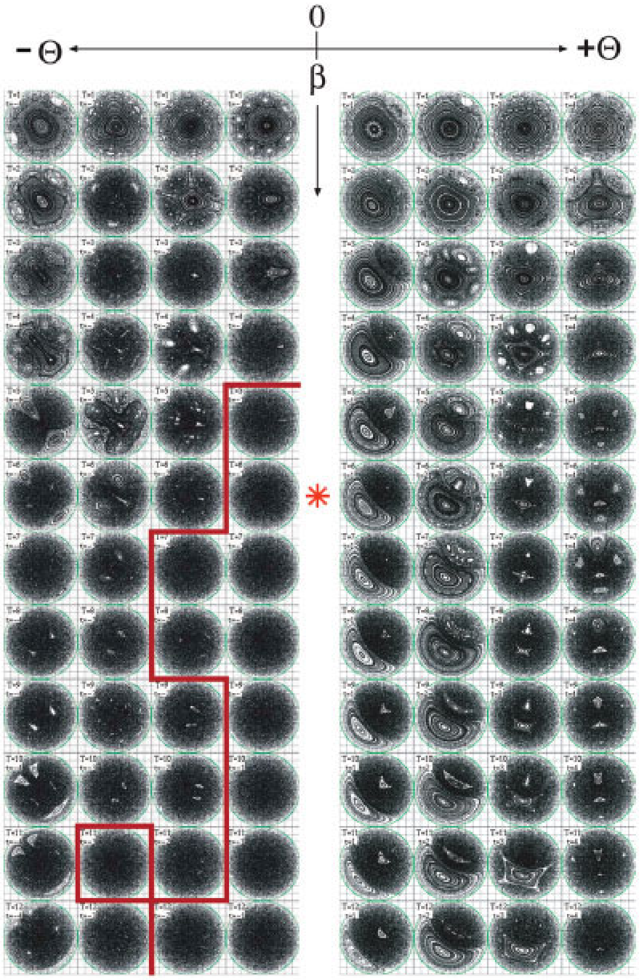

Figure 5. Poincaré sections in the $(\beta - \Theta)$ plane for Newtonian Stokes flow, analytic in-plane and axial solutions.

$\Delta = \pi/4$. Boxed regions show parameter regions of potentially good mixing. The $*$ indicates the two states in the experiments of Figure 8.

4. Once a promising region in parameter space is selected, refine and check with dye tracing. Figure 6 shows an example of a dye trace, which reveals good mixing can require not much more than 10 RAM windows. The figure also shows the basic progression of the mixing. The initial condition $(N = 0)$ is a disc of fluid, half of which is red and half black. The subsequent images show the location of the same particles as they pass the end of the Nth window. The basic mixing mechanism, the swirl caused by the moving boundary at the window, is clearly visible. This basic flow stretches the fluid and is reoriented at every subsequent window, repeatedly stretching the fluid from different orientations.

5. If desired, refine further by calculating stretching distributions. Figure 7 shows an example of a stretching plot. This plot was done over the entire (β, Θ) plane as an exercise. Light colors are higher average stretching; dark colors are low average stretching.

6. With values for β and Θ in hand, manufacture the predicted RAM inner cylinder.

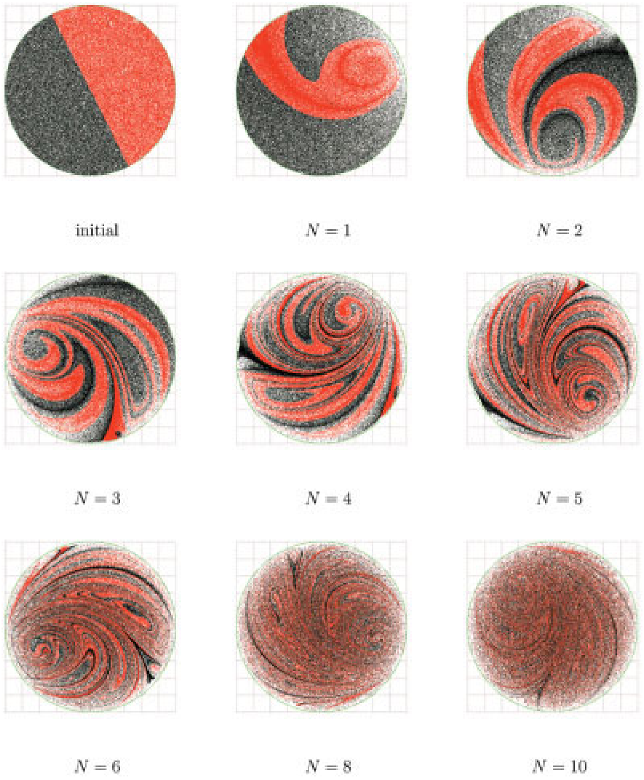

Figure 6. Mixing progression for a Newtonian fluid.

Computational dye traces shown after N RAM windows showing the repeated stretching and reorientation of the flow. Flow parameters correspond to the experiment in Figure 8.

Is this procedure to find globally chaotic, well-mixed solutions guaranteed to succeed for any fluid? Probably not. However, for all the examples of generalized Newtonian model fluids that we have examined, such robust solutions have been found for values of β that also make them practical to build.

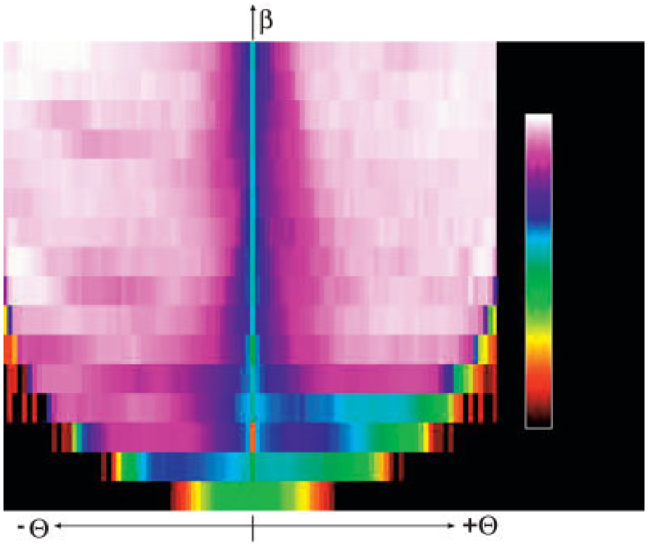

Figure 7. Stretching plot over the (β, Θ) plane for Newtonian fluid for fixed total energy input.

Light colors are higher average stretching; dark colors are low average stretching.

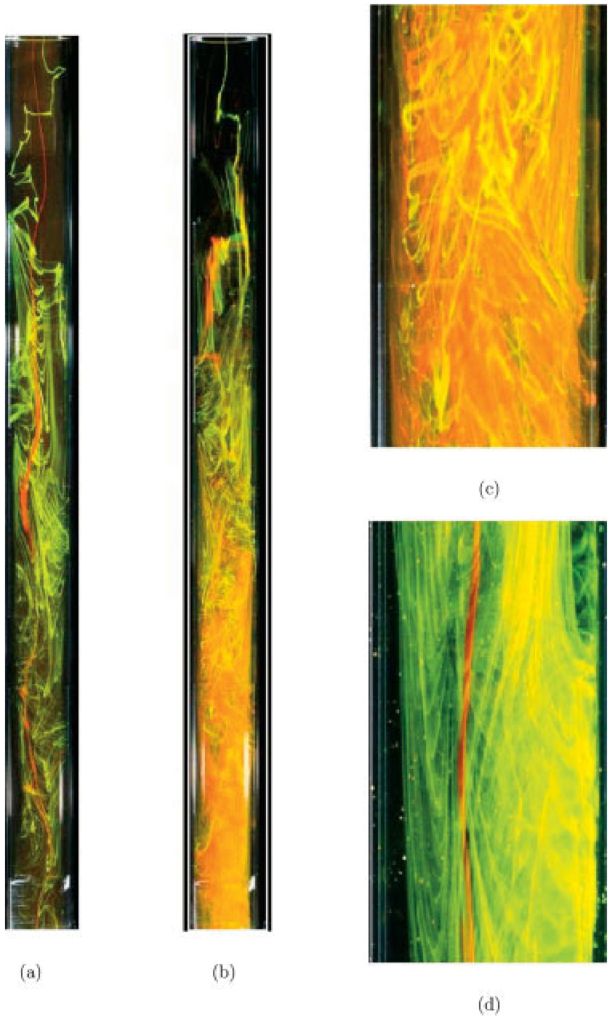

Figure 8. Experimental examples of good and poor mixing from different parts of RAM parameter space, c.f. Figure 5.

Red and green dye streams are injected at the top of the figure. The main flow is from top to bottom. (a) shows a poorly mixed case; (d) is a closeup of (a). The green dye mixes well, but the red dye was placed in an "island" and passes through the duct unmixed. (b) shows a well mixed case; (c) is a closeup of (b).

Figure 8 shows the results of two experiments to validate the computational model and the dynamical sieve procedure. The working fluid and the two dye streams are 90% glycerol-water solutions. The fluids and experiment were prepared as described earlier. At all times the flow is steady and laminar with $Re = 4$. Figures 8a and b show the full length of a RAM tube section of 15 windows. Flow is from top to bottom. Two dye streams, red and yellow, are injected prior to the RAM section inlet at the top. Figures 8c and d are closeups of respectively b and a three quarters of the length down from the inlet. Figures 8b and c show the globally well-mixed solution found through the sieve procedure. By the end of the 15 windows the two dye streams are globally dispersed and well-mixed, as predicted.

Figures 8a and d show the same experiment with a different

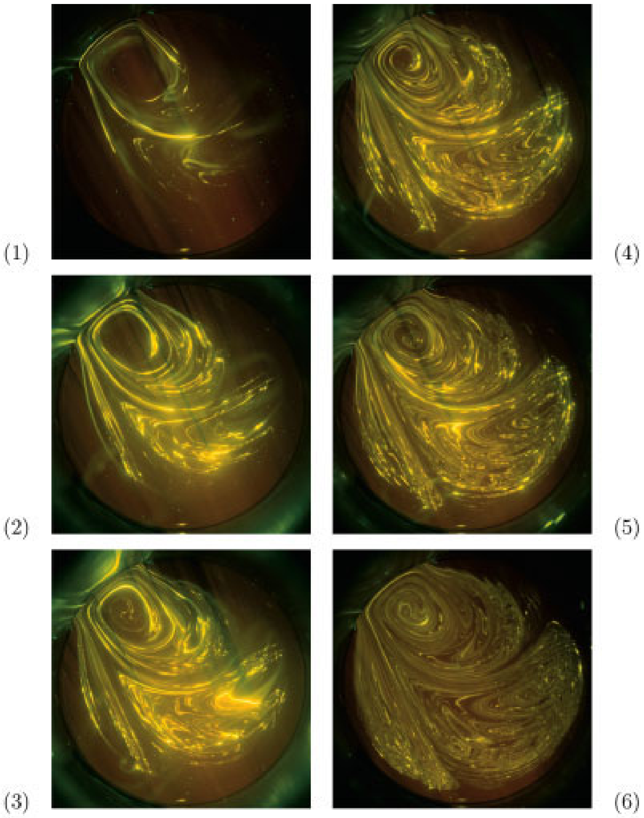

Figure 9. Sequence of images used to measure the residence-time distribution.

A laser sheet perpendicular to the flow illuminates UV fluorescent dye as it passes a RAM window. Regions outside the fluid were removed from the RTD measurement.

sense of rotation of the outer cylinder. The symmetries of the flow are such that reversing Ω is equivalent to $\Theta \rightarrow -\Theta$. The rotation of the outer cylinder in a direction opposite to the offset (counter-rotating case) results in good mixing, and in contrast, rotation in the same direction as the aperture offset (co-rotating case) is predicted to result in poor mixing with a large island taking up a large volume of the flow. Consulting Figure 5, we see the two marked predicted flows corresponding to the two experiments. By changing the sign of Θ, reversing Ω, the predicted solution changes to one with a large island. This verifies that the computational procedure is correctly predicting more complicated structures available in the experiments.

Residence-Time Distribution

The well-mixed RAM solution can be further characterized by its residence-time distribution (RTD). We measure the RTD as described earlier by placing many small blobs of dye in an initial plane at the inlet and by cutting the flow with a laser sheet perpendicular to the axis after the last window boundary. As the finite amount of dye flows through the laser sheet we record the dye image intensity with a digital camera. The time record of the integrated image intensity then gives the RTD measurement. Figure 9 shows examples from the sequence of images. Figure 10 top shows the RTD data as points with a numerical RTD, initialized as in the experiment, drawn with a solid line. In the figure time is normalized to the mean residence time $t^* = V/Q_v$ calculated as the RAM volume over the volume flow rate, and the computational data is scaled only in height to match the intensity units of the experimental data. The faster fall-off of the data compared to the computation is an experimental artifact due to the nonlinear response of the

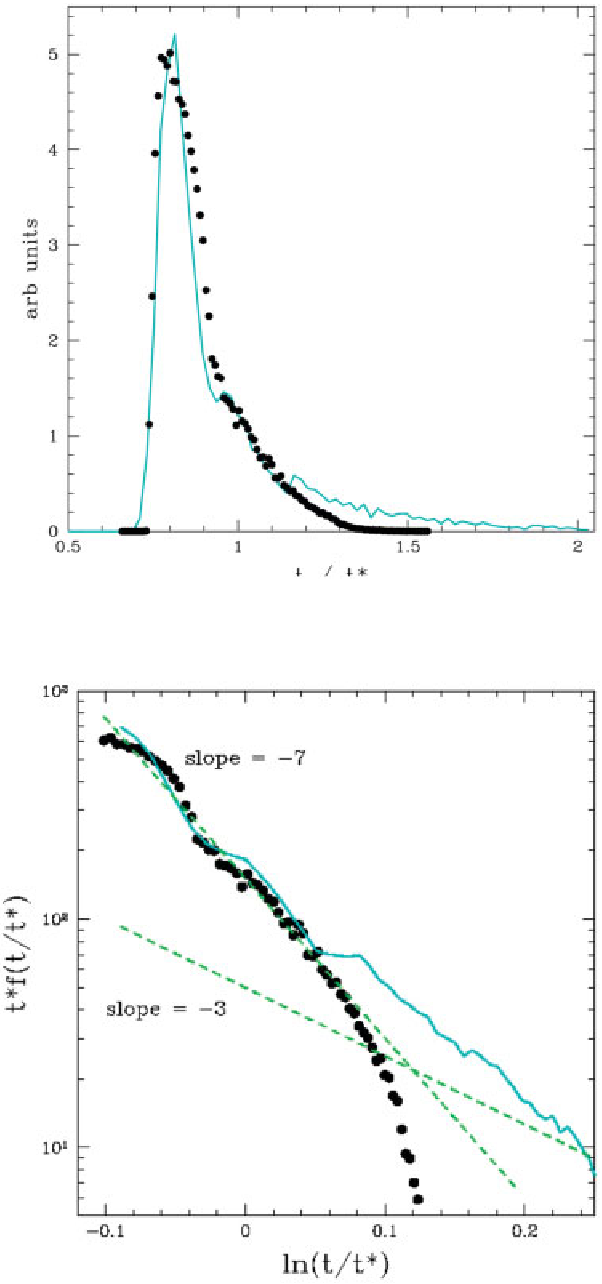

Figure 10. Residence-time distribution for a RAM global mixing case.

(Top) points are image intensity measurements from images like those in figure 9 and the solid line is from computation. Time is scaled by the mean residence time t^*. (bottom) RTD data normalizing the area under the curve to one plotted log-log. The dotted line of $(t/t^*)^{-7}$ follows the initial falloff of the data. The dotted line of $(t/t^*)^{-3}$ falloff is the long time theoretical expectation for diffusion-free, noslip systems.[48]

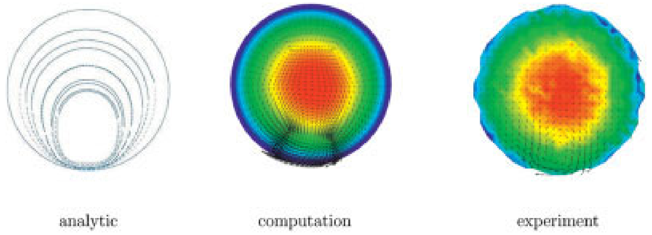

Figure 11. Velocity field at the center plane of a window.

Analytic is the 2-D Stokes flow solution of Hwu et al.[45] for flow in a circle driven by a moving boundary arc.

The computation and experiment are 3-D RAM flows at $Re = 4$. Arrows indicate the in-plane velocities, whose maximum is at the moving boundary at 6 o'clock. Color indicates the axial velocity, whose maximum is at the centerline.

camera at low fluorescence intensities, as most of the dye at these times has passed out of the device.

RTD theory is a well-developed subject and a few remarks relating the RAM data to standard results may be illuminating. The lower part of Figure 10 shows the raw data as a normalized probability density function $f(t)$. Theoretical predictions for f for several flows interesting to compare to the RAM results are given by Nauman and Buffham.[48] For a plug flow $t^*f(t) \propto \delta(t/t^* - 1)$, where $\delta(0) = 1$ and equals 0 otherwise. For a perfectly mixed stirred tank $t^*f(t) \propto \exp(-t/t^*)$. And for laminar pipe flow $t^*f(t) \propto (t/t^*)^{-3}$ for $t/t^* > 1/2$, where the time in the inequality is called the first appearance time. The first appearance time for the RAM data is about 0.75, which, perhaps coincidentally, is the same as is predicted for a single screw extruder.[48] Between plug flows and perfect mixers are tanks-in-series models where $t^*f(t) \propto (t/t^*)^{\bar{N}-1}\exp(-\bar{N}t/t^*)$, and $\bar{N}$ is the number of stirred tanks in series. These models are "in between" because $\bar{N} = 1$ recovers the result for a single stirred tank, while as $\bar{N} \to \infty$ the RTD distribution approaches that of plug flow. When plotted log-log the initial fall-off of the RAM RTD data follows $(t/t^*)^{-7}$, which is much faster than for laminar pipe flow alone. The dotted line of $(t/t^*)^{-3}$ falloff is the long time theoretical expectation for diffusion-free, noslip systems.[48] If we fit the data to a tanks-in-series model with $\bar{N}$ the only free parameter, we find $\bar{N} = 16$. Pushing the conclusions that can be drawn from comparisons of this data to RTD theory, it suggests that after some initial startup length approximately every 2 RAM windows is equivalent to a well-stirred tank.

Velocity Fields and Inertial Effects

The velocity field of the RAM is simple and easily measured by LDV. The moving boundary arc produces a circulation added to the axial flow. Rheology or inertia can couple the in-plane and axial velocity components, particularly around the boundaries between windows. In this section, we first compare measured and computed velocity fields and look at the influence due to inertia of motion in one window cell on its up- and down-stream neighbors. Then we show the effects of increasing inertia on the advection field from Stokes flow up to $Re = 10^3$.

Figure 11 shows in-plane and axial representations of the RAM velocity field in a plane perpendicular to the duct axis in the center of a window far from the duct inlet or outlet. The analytical streamline solution is the 2-D Stokes flow solution of Hwu et al.[45] for flow in a circular domain driven by a moving boundary arc. Next to it is our numerical 3-D RAM computation for $Re = 4$. The arrows are in-plane velocity vectors, which have a maximum value at the moving boundary at 6 o'clock. The axial velocity component is color coded with its maximum value along the centerline of the pipe. The axial flow for this Newtonian fluid model closely follows a Poiseuille pipe profile. The hexagonal symmetry is a visual artifact of the computational grid. On the right are our LDV measurements for $Re = 4$. Arrows and colors denote the same quantities as for the computation. The raggedness is due to optical imperfections in the acrylic, rotating outer tube that causes slight wobbles in the laser beams. The agreement between the Stokes flow solution, computation, and experiment is excellent.

The agreement between experiment and computation is amplified in Figure 12, which shows data for $Re = 10$. The experimental and computational domain is a single RAM window: there are no other windows in the tube, and the window is far from the inlet and outlet. For the figure we have summed the in-plane kinetic energy $K_{cs} = 1/2 \sum_i (v_r^2 + v_\theta^2)_i$ at each grid point and normalized K_{cs} to its maximum value in the window, and plotted K_{cs} vs. the distance along the axis z in units of pipe diameters. In the ideally decoupled case all the in-plane motion would be confined within the window. The solid line in the figure is computational data; the dots are experimental data; and, the vertical dotted lines mark the window boundaries. Axial flow is from $+z$ to $-z$. The agreement between experiment and computation is still

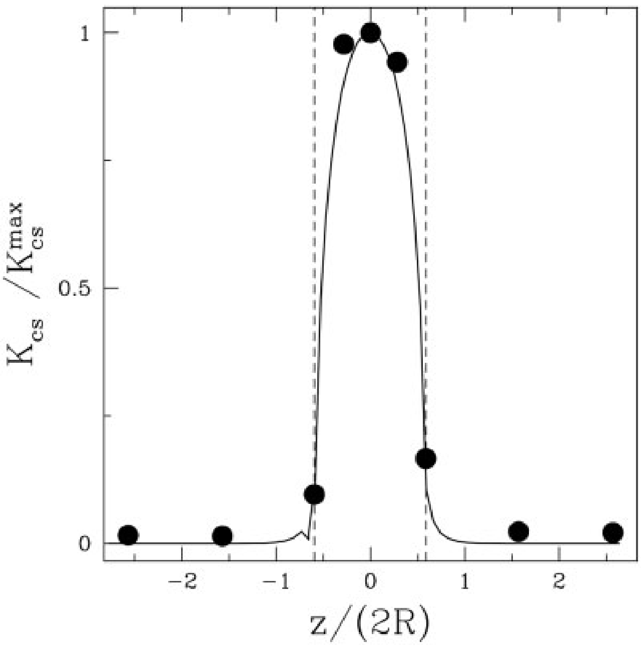

Figure 12. In-plane kinetic energy K_{cs} (normalized to its maximum value) versus axial distance z (in units of pipe diameters) around a single RAM window (with the origin at the center of the window) for a Newtonian fluid and $Re = 10$.

Solid line is computation and dots are experiments; dotted lines show the window boundaries. Axial flow is from $+z$ to $-z$.

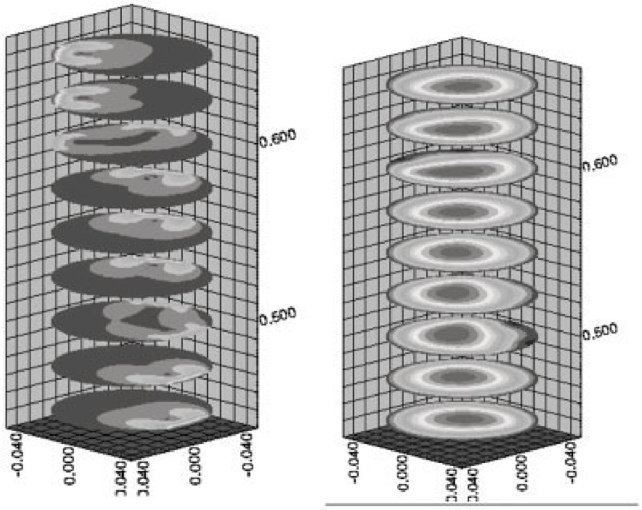

$Re = 10$

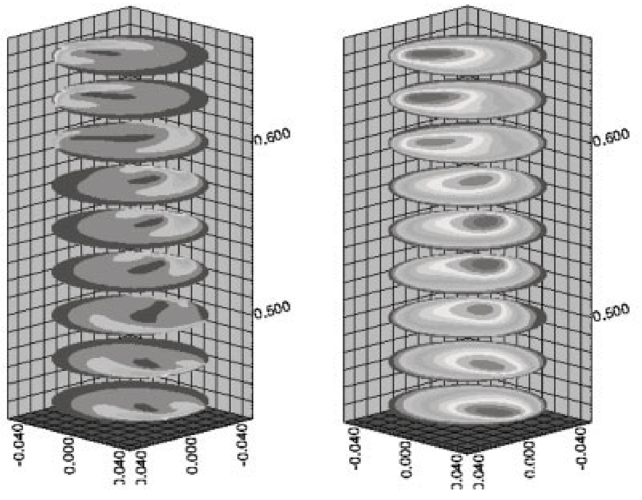

$Re = 100$

Figure 13. Computed 3-D velocity fields at several planes over an entire RAM window for Reynolds number of (a) $Re = 10$, and (b) 100.

On the lefthand side the gray scale gives the magnitude of the in-plane velocity, while on the righthand side the gray scale gives the axial velocity. In-flow and out-flow window boundaries are at 0.5 and 0.6 respectively. Axial flow is from top to bottom.

excellent. For Reynolds numbers up to a few tens inertial effects and "spinup" of neighboring cells is confined to a small distance around the window boundary of not more than $0.2H$ in length. A similar plot of the axial kinetic energy would show a straight line with barely noticeable wiggles at the window boundaries. This is the situation up to Reynolds numbers around 50.

However, with further increases of Re inertial effects become significant. Figure 13 shows 9 planes of computed velocity fields for $Re = 10$ and 100. Axial flow is from top to bottom. Window boundaries are at $z = 0.5$ and 0.6. On the left are the in-plane velocity components color-coded such that light denotes large velocities and dark small velocities. On the right are planes of the axial velocity component with the same relative color-coding. At $Re = 10$ the changeover from one orientation to the next of the in-plane velocity takes place at the window boundaries and essentially nowhere else. This is clearly the case with the in-plane components. The axial component has a small region near the boundary between moving arc boundaries where the fluid slows down. This generates a small pressure and pushes the maximum velocity slightly off the centerline. Note too the slight up- and down-stream asymmetry of K_{cs} in Figure 12. All these inertial effects are of course magnified in the computations for $Re = 100$. Here the in-plane azimuthal components near window boundaries are markedly asymmetrical with the effects extending much farther outside the window boundaries, especially downstream. The axial velocity is no longer Poisieulle-like as the maximum velocity now spirals around the centerline.

These effects are quantified in Figure 14. In the same manner as figure 12, in Figure 14 (top) we plot the in-plane kinetic energy along the axis for $Re = 10^{-2}$, 1, 10 and 10^2. Thicker lines correspond to larger Re, and the lines at $Re = 10^{-2}$ and 1 lie on top of each other. There is an up- and down-stream asymmetry that increases markedly with increasing Re. Figure 14 (bottom) plots the integral of K_{cs} taken outside the window normalized by the integral of K_{cs} over all z vs. the largest Re (in-plane or axial). This quantifies the extent of "cross-talk" between windows due to inertia. For $Re < 50$ this cross-talk involves around 10% or less of the total energy of in-plane motion, but rises with further increases in Re.

A further important question is the effect of inertia on the advection field. In Figure 15 we show Poincaré sections for two complementary values of Θ (all other kinematic parameters the same) as Re increases from 0 to 10^3. On the right at low Re kinematic parameters are set to give a well-mixed case, while on the left the change of sign of Θ gives rise to one large island. In this case the topology remains similar through Re of about 50. By $Re = 100$, though the advection topology has changed. In both cases more elliptic points, corresponding to extra islands, appear and remain for further increases to Re.

Comparisons of Mixing Effectiveness

With the RAM flow defined and characterized and with methods to interrogate the chaotic advection field, we turn to the question of comparing the RAM's globally well-mixed optima with other mixers, both static mixers and other mixers for viscous liquids. The RTD measurements earlier are one way to characterize and compare the RAM mixing effectiveness with other devices and with data in the literature. In this section we derive the required power inputs,[1] compare mixing performance, and examine the dominant character of the RAM mixing flow through a measure of its efficiency.

Power

In-line mixers usually have internal elements such as baffles and plates which increase the pressure drop required to drive

---

[1] As we are interested in low Re mixing, comparison between high-energy input turbulent mixing and relatively low-energy input chaotic laminar mixing is beyond the scope of this paper. However, Raynal and Gence[49] have given a general argument comparing turbulent and chaotic mixing, concluding that at higher Schmidt numbers global chaos is *always* more efficient (energy input for equally well-mixed) than turbulent.

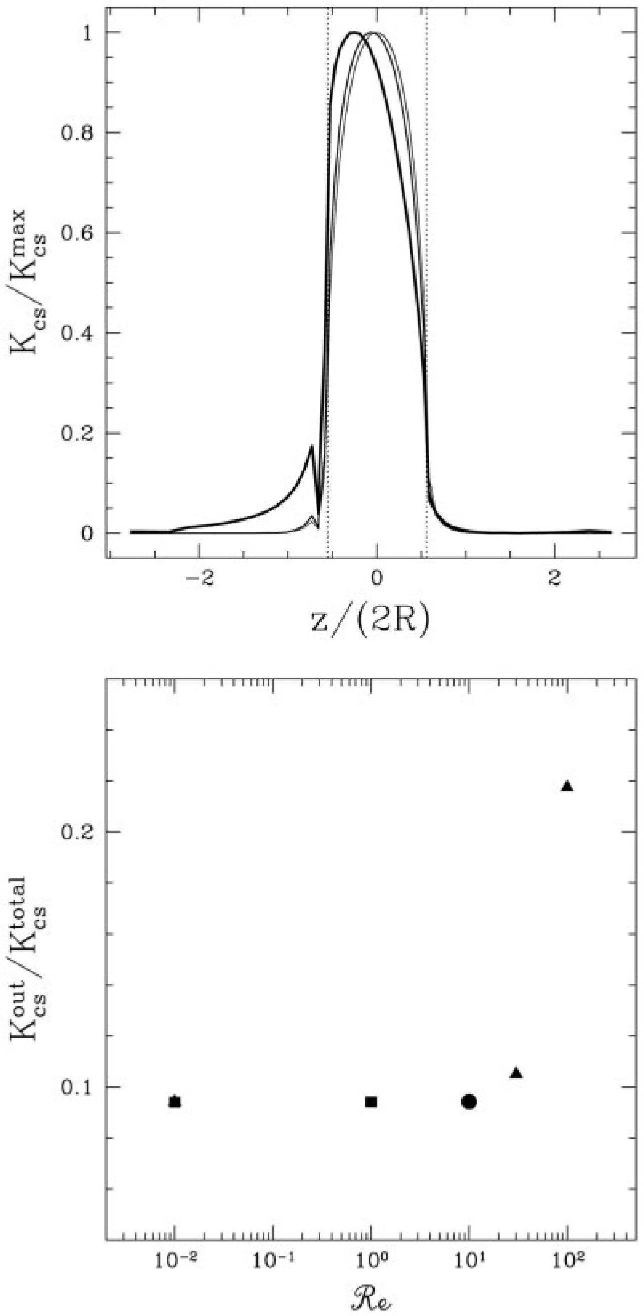

Figure 14. Window-to-window "cross-talk" as a function of *Re* computed for a Newtonian fluid in a single window RAM.

(top) Plots of in-plane kinetic energy normalized to its maximum value vs. axial distance z in units of pipe diameters with the origin at the center of the window. Vertical dotted lines are window boundaries; axial flow is from $+z$ to $-z$. Lines thicken with increasing $Re \in (10^{-2}, 1, 10, 10^{2})$. Lines at $Re = 10^{-2}$, 1 are indistinguishable. (bottom) The amount of in-plane kinetic energy outside the window (normalized to the total in-plane kinetic energy) as a function of maximum Re.

fluid through the mixer and provide surfaces on which fouling and scale can potentially grow. Pumping power P_{ax} required is the pressure drop ΔP times the volume flow rate Q_v, and, as Q_v $\propto \Delta P$, $P_{ax} \propto (\Delta \mathrm{P})^2$.[2] Table 1 lists the pressure drop for several duct mixers, with ΔP in units of the pressure drop of an open circular pipe.[2] In these units the RAM clearly has a pressure drop of 1. For comparison there are listed two commercial static mixers, for which we have been able to find data; the Kenics data is from Pahl and Muschelknautz[50] and the SMX data is from Streiff et al.[19] Unsurprisingly the static mixers with their internal flow impediments have significantly larger pressure drops.

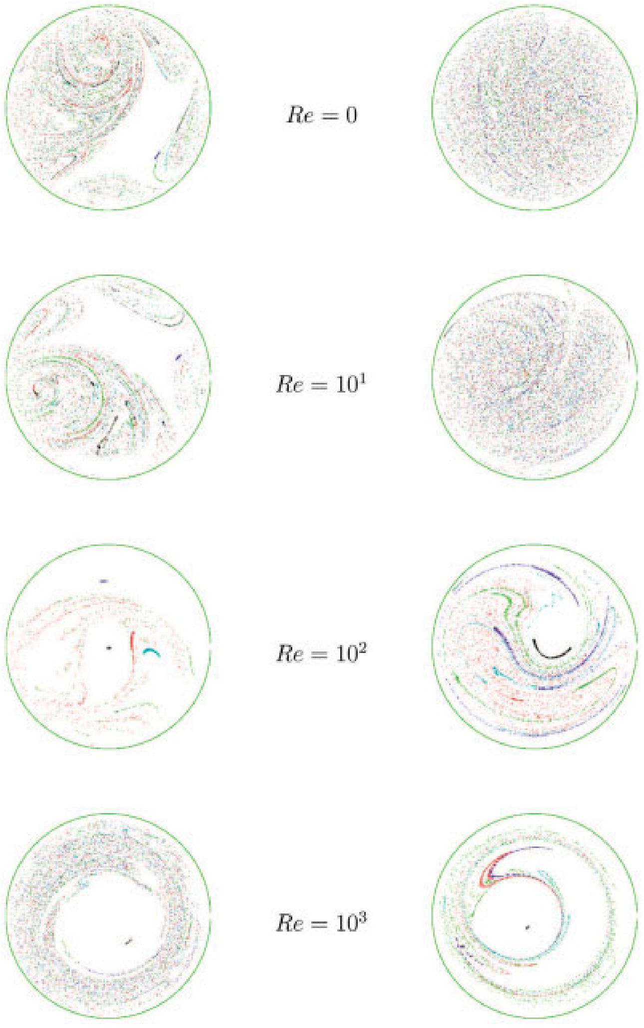

Figure 15. Poincaré sections for increasing *Re* in a Newtonian fluid. Columns show two values of Θ marked by the "*" in Figure 5 and the experiments of Figure 8.

However, a fair comparison considers total energy inputs. For static mixers total energy is only ΔP, while for the RAM we must add in the rotational energy P_r, which is derived in the appendix as

---

[2] Data are for Newtonian fluids. For shear-thinning fluids the window shear flow should cause a local viscosity reduction and consequently, for a given flow rate, a lower pressure drop for a RAM. This effect of shear rate profile complicates pressure drop comparisons between the RAM and static mixers for power-law fluids, though direct measurements of pressure drop would be straightforward. We thank an anonymous reviewer for bringing this point to our attention.

Table 1. Pressure Drop ΔP, Total Power Input P, and Striation Reduction Rate m for the RAM and Two Commercial Static Mixers

	ΔP	P	m
RAM	1	1.1–3	0.41
Kenics	6	6	0.30
SMX	37	37	0.43

Pressure drop and power for Newtonian laminar flow are normalized to their values for an open pipe. For the RAM and the Kenics m is a fit of $\exp(-mz/(2R))$ to the data of Figure 16; for the SMX, m is taken from Streiff et al.[19]

$$P_r = \chi \mu L (\Omega R)^2 \Delta \tag{5}$$

where χ is a dimensionless prefactor that is calculable in principle, but in practice is empirically determined. The required rotational power input for chaotic advection can be small. For a window opening of $\Delta = \pi/2$, $\chi \sim 30$. Further assuming $\mu \sim 10$ Pa-s, $L \sim 1$ m, $R \sim 0.05$ m, and $\Omega \sim 1\ \mathrm{s}^{-1}$, then $P_r \sim 1$ Watt.

In order to compare total power input P across devices on the same basis as we did with pressure drop, we want to scale P by P_{axt}, the axial pumping power required for an open tube. (Details of the scaling are in the Appendix.) Assuming a Poisieulle profile to calculate flow rate and recalling the definition of β, we find

$$P = 1 + \frac{\chi}{32\pi}\left(\frac{\beta}{\Gamma}\right)^2 \tag{6}$$

Assuming the same values as earlier, and noting the empirical result that $\beta \sim 10$ for a globally well-mixed solution, and $\Gamma \sim 10$, then the nondimensionalized total power input is $P = 1 + \mathcal{O}(1)$. In practice, for the RAM we find $P \in [1.1, 3]$. Comparisons of the total power input for the RAM and two commercial static mixers is in the second column of Table 1. The RAM requires considerably less power input than conventional duct mixers.

Performance

The RAM uses less energy to perform than some comparable devices. For a given power input how is the mixing performance? Figure 16 shows computed data for three mixers—we are not aware of similar experimental data—for the average striation size reduction as a function of length z down the duct.

Byrde[51] and Byrde and Sawley[52] considered the flow in a Kenics style mixer with offset helical twists. They defined a measure of mixedness from the dye pattern formed at a plane placed in the flow after each helical insert (that is, from simulated data similar to the experimental photos of Figure 9) and a "structural radius" defined at each point on this plane. The structural radius at point x is the radius of the largest circle which contains only fluid of the same type as at point x. The mixing measure s is the structural radius averaged over all points in the plane; s is a measure of average striation thickness.[3] Though clearly not the only measure that could be defined, s allows mixing to be quantified from simulations and comparisons of different mixers to be made. The Kenics simulation data are the squares in Figure 16. The simulation data for the RAM, the circles in Figure 16, uses the same mixing measure s. The thick line in Figure 16 is the striation reduction correlation for an SMX static mixer given by Streiff et al.[19] The thick line is $l/l_0 \propto \exp(-mz/(2R))$ with the striation reduction rate $m = 0.43$ for an average striation size l and initial size l_0. Fits of this exponential form to the Kenics and RAM points are the thin lines. All three mixers exponentially reduce striation thickness, and m for each is tabulated in Table 1.

While there are many static mixers for which we have no comparable data for energy use and striation reduction rate, for the available data we can see that in one case (for a fixed length) the RAM mixes about twice as well for about 1/5th the energy use ($P = 1.2$ for the RAM computation in Figure 16), and that in the other case the RAM mixes slightly less rapidly for about 1/30th the energy use.

Efficiency

The final comparison is for the predominant flow type. Most mixing flows are shear dominated. High shear rates and shear stresses do the work of mixing and dispersion. However Figure 17 shows the RAM flow is predominantly low shear. The inset of Figure 17 plots the local shear rate—calculated as the norm

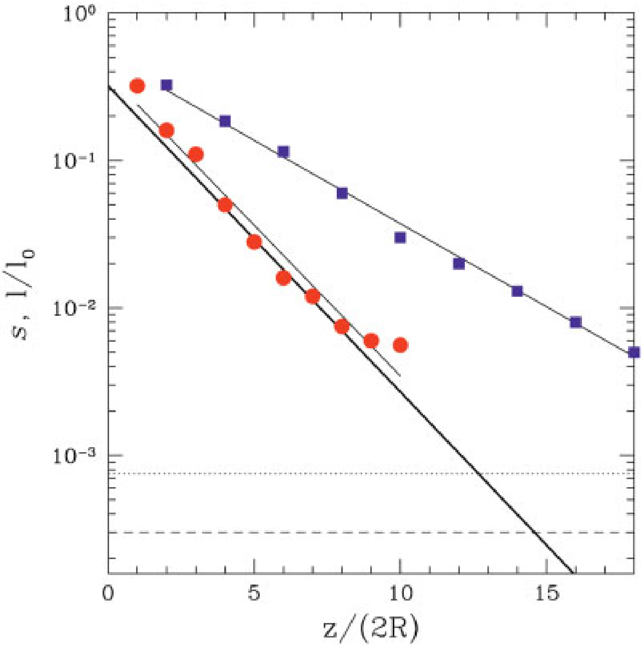

Figure 16. Mixing comparison of the RAM to several static mixers.

Length of the continuous mixer sections are in units of RAM window lengths. Normalized structural radius s, defined in the text, is a measure of striation thickness. The squares are Kenics data from Byrde[51] and Bryde & Sawley.[52] The circles are data from RAM simulations. The dashed horizontal line is "perfect" mixing, as measured by s, and the dotted horizontal line is the 99th percentile of perfect mixing. After approximately 8 apertures, the measure flattens out for the RAM due to numerical limitations associated with the number of particles used in the simulation (20 times fewer than the Kenics simulation). The thick line is the striation length, l/l_o, reduction correlation of Streiff et al.[19] for an SMX static mixer.

---

[3] Although s is limited by the initial number of particles n used in the simulation and asymptotes to a fixed value proportional to $n^{-1/2}$.

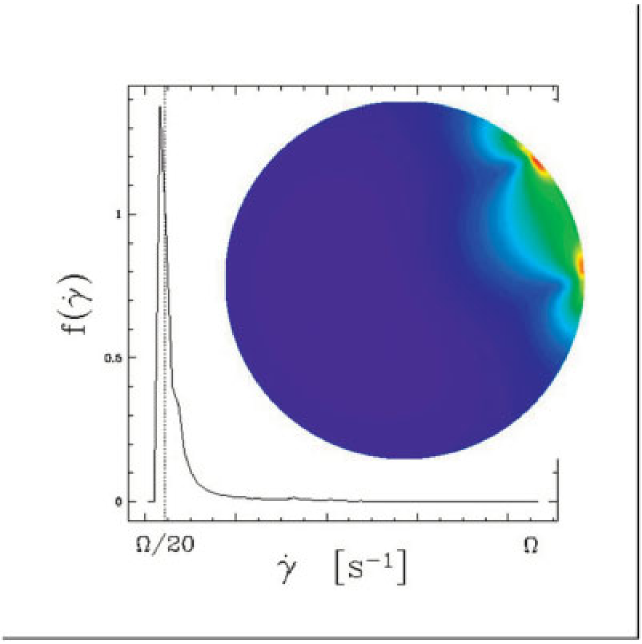

Figure 17. Shear rate distribution. Shear rate $\dot{\gamma}$, calculated as the norm of the velocity gradient tensor, distribution over the in-plane space of the RAM flow.

Light colors are high $\dot{\gamma}$, which occur at window edges. The graph is a normalized frequency distribution of $\dot{\gamma}$, which is normalized to the rotation rate Ω. The dotted line at $\dot{\gamma} = \Omega/20$ is the distribution median.

of the velocity gradient tensor—over the cross-section of the RAM flow. Light color shows high shear rates, which are confined to the windows' azimuthal boundaries. The graph in Figure 17 is the normalized frequency distribution of shear rate. The bulk of the flow, including along most of the window boundary, experiences a nearly constant shear rate that in magnitude is around Ω/20. So the RAM flow is low shear, but the mixing data shows the RAM mixes well. The answer to this seeming puzzle is that the RAM is dominated by elongational flow.

To see this predomination of elongational flow in the RAM, consider Ottino's[2] measure of mixing efficiency e_λ, defined as the local stretching rate normalized by the local shear rate, $e_\lambda = (D(\ln \lambda)/Dt)(\mathbf{D} : \mathbf{D})^{-1/2}$, where λ is the local stretching, D/Dt is a convective derivative, and $\mathbf{D}$ is the deviatoric stress tensor. Physically e_λ is the locally dissipated energy that goes into stretching. For a pure shear flow e_λ approaches an upper bound of $e_\lambda < 0.71$ at some time, after which e_λ decays asymptotically as t^{-1}. For a 3-D pure elongational flow e_λ has a constant upper bound of $e_\lambda < 0.82$. Of the two, elongational flow is the more efficient stretching flow, which agrees with our intuition. Of course, real flows are not purely one or the other, but shear or elongation can predominate and determine the character of an overall flow.

To calculate e_λ for the RAM we take $D(\ln \lambda)$ from the inverse of the striation reduction data in Figure 16, that is, $D(\ln l_o/l)$, averaged over each window segment, and take Dt as the average residence time from the definition of β, and the average shear rate from Figure 10:

$$e_\lambda = \frac{\Omega D(\ln l_o/l)}{2\Gamma\beta\dot{\gamma}} \tag{7}$$

Taking averages with $\langle \Omega/\dot{\gamma} \rangle = 20$, $\Gamma = 8$, $\beta = 5$ and $D(\ln l_o/l) = 3.2$ averaged over the data points in Figure 16, $e_\lambda = 0.80 \pm 0.02$ with the variance coming from the window to window scatter in the points of Figure 16. Though not calculated, the other mixers in Figure 16 would have lower e_λ due to either lower average stretching rate or higher average shear rate. That this efficiency is close to the elongational maximum and does not decay suggests that the RAM flow is predominantly elongational.

Generalized Situations

In many practical applications, highly viscous non-Newtonian fluids must be mixed with other fluids and/or particulates. Each different rheology may have a different robust, optimum operating point in the RAM parameter space. There are few studies of chaotic advection of non-Newtonian model fluids; for example, see the experiments and computations by Niederkorn and Ottino[53,54] and computations by Fan et al.[55,56] In this section, generalized mixing situations of shear-thickening fluids, of shear-thinning fluids, and of Newtonian fluids with large viscosity differences will be briefly considered to highlight the utility of the RAM in a range of mixing applications.

Shear thickening fluids

Methyl-cellulose is an example of a shear thickening fluid. Fitting a power-law model of the form $\mu = \kappa\dot{\gamma}^{(n-1)}$ to available rheology data gives $n = 1.85$ and $\kappa = 1$ Pa-s$^{(-n+1)}$, and this model was used for advection computations. The method of the design section to find a robust mixing optimum was followed and a set of RAM design parameters chosen. For shear thickening fluids it appears that globally chaotic regions of parameter space are common, although the aperture length needs to be somewhat longer than found for Newtonian fluids. The numerical dye traces in Figure 18 show the initial condition and mixing patterns after 2, 4 and 8 apertures. Note that there are regions near the wall seemingly deficient in particles. These regions of the flow do mix, but more slowly than the rest of the flow: RTD measurements would show a longer tail.

Shear thinning fluids

Shear thinning fluids occur for a wide range of mixing applications. They are generally more difficult to mix than Newtonian and shear thickening fluids, because the shear induced in the neighbourhood of an aperture by the motion of the outer cylinder reduces the viscosity of the fluid and the perturbed flow penetrates less deeply across the inner cylinder of the RAM. This difficulty occurs not only in the RAM, but for all other chaotic and turbulent mixing methods. In the RAM it is common to find large nonmixing islands, such as those seen in the Poincaré section on the left of Figure 19. The calculation is for a shear thinning fluid of shear index $n = 0.29$, which is more shear thinning than typically encountered in applications, and consistency $\kappa = 15.5$ Pa-s$^{(n-1)}$, using the power-law rheology model above. A robust solution for removing these persistent islands is to add an additional offset every 3–6

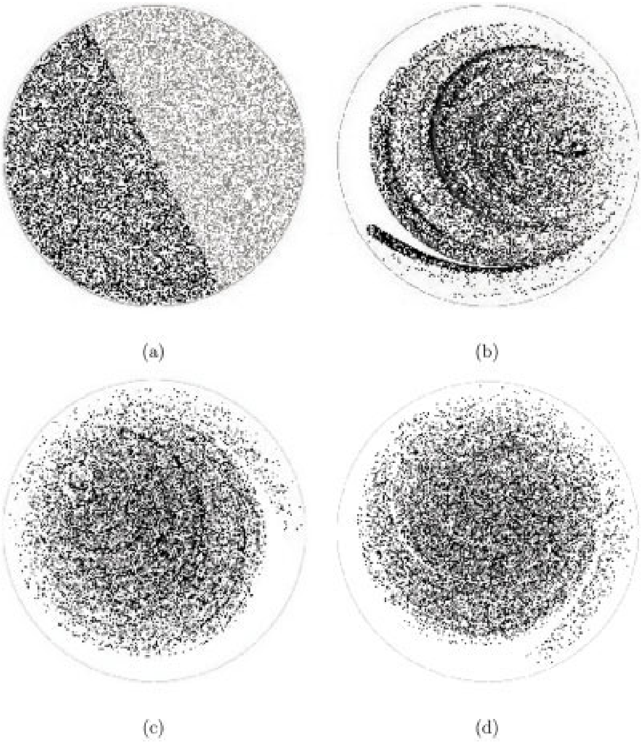

Figure 18. Dye traces for a shear-thickening fluid of shear index n = 1.85 and consistency κ = 1 Pa-s$^{(-n+1)}$.

(a) Initial fluid distribution, (b) distribution after 2 apertures, (c) after 4 apertures, and (d) after 8 apertures.

apertures that breaks the symmetry and moves the nonmixing region into a chaotic region. An example of the effect of this procedure is shown in the image on the right of Figure 19. Here, the effect of an additional offset of $\pi/2$ every four apertures once again produces a globally chaotic mixing flow. Although this procedure results in overall slower mixing (more windows and longer ducts) than otherwise, it still results in effective mixing for a fluid that is by any means difficult to mix.

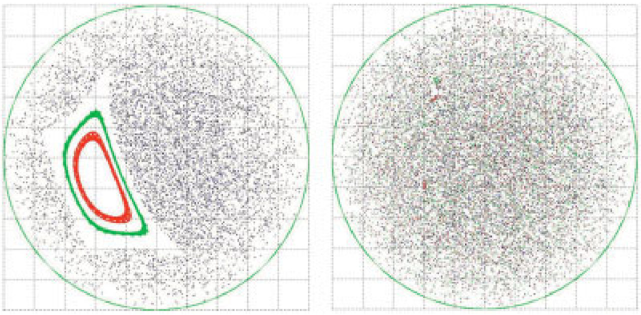

Figure 19. Poincaré sections for a shear-thinning fluid of shear index n = 0.29 and consistency κ = 15.5 Pa-s$^{(-n+1)}$.

(Left) using a uniform aperture offset. (Right) using a uniform offset plus a second offset of $\pi/2$ every four apertures.

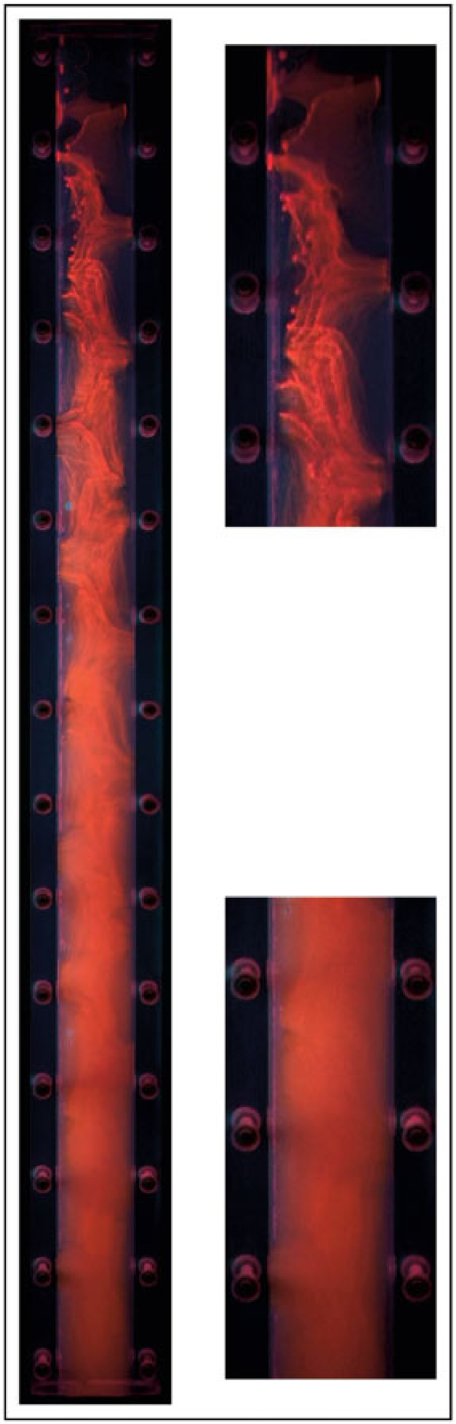

Figure 20. Experiment mixing a low viscosity additive.

The viscosity ratio of the additive to the major component is 5×10^{-3}. Experimental parameters are similar to the good mixing case of Figure 8. Flow is from top to bottom; however, the experiment had horizontal flow and gravity points left to right. On the right are choseups of the beginning and final 20% of the RAM duct.

Large viscosity differences

Particularly in polymer applications low viscosity additives are often blended into high viscosity fluids, where the viscosity difference can be several orders of magnitude. Figure 20 shows an example of such an experiment. The red dye stream is a glycerin-water mixture that is about 2% of the total volume flow; the main stream is pure glycerin, such that the viscosity ratio (measured using a Bohlin rheometer) of the additive liquid to the main liquid is 5×10^{-3}. The control parameters are set for the globally chaotic flow found in the design section. Flow is from top to bottom in the picture; however, the experiment had horizontal flow and gravity points left to right in Figure 20. The left of Figure 20 shows the entire duct; the two photos on the right show closeups of the beginning and final 20% of the duct. By the end of the mixing section the additive has been blended to the diffusion limit. In-plane observation shows no discernible features in the uniformly mixed dye additive.

Note that dye near the duct entrance rises to the top of the inner tube, while dye further along does not reach the top in the same time. The further along the duct, the more slowly the dye rises, until about 25% along the duct, there is no discernible rise after more than 12 h. What's happening is that as dyed striations become thinner and thinner, the density difference between any given blob of fluid, and the surrounding fluid is eliminated, another, albeit indirect, measure of mixing performance.

Conclusions and Discussion

Laminar blending is essential in many applications. The effective way to accomplish this blending is via chaotic advection. We have described the continuous, open duct *Rotated Arc Mixer* flow and some of its chaotic states by experiments and computations. Key characteristics of the RAM are the existence of several control parameters, allowing tuning of the chaotic advection and flexibility in application, and the lack of internal elements, making its pressure drop the same as an open pipe. Being predominantly elongational in nature, the flow in the RAM is low shear. The operating principle uses a deterministic sequence of boundary manipulations on the RAM duct walls, generating programmed sequences of flow reorientation and allowing us to compose various distinct chaotic flows depending on the material parameters and fluid rheologies. We have described efficient numerical dynamical systems methods to look for desirable chaotic operating designs throughout the, possibly large, control parameter space.

The RAM flow may be advantageous for applications for any of several reasons, including

- Blends well in low Reynolds number situations, that is, high viscosities and/or small length scales,
- No internals, so a low pressure drop, simple cleaning, cost effective manufacture, no surfaces to clog or for scale to build up on, and no stagnant regions,
- Can be optimized for different fluid rheologies,
- Has low shear with effective mixing, predominantly elongational flow, a low work input to materials being mixed,
- Mixes as well or better than static mixers at the same flow rate for substantially lower energy input,
- Design process and scaleup can be simpler than for static mixers or stirred tanks.

We have shown a few uses of the RAM for non-Newtonian and low viscosity additive blending, but prospective uses are for any low *Re* application. For instance, chaotic flows can decouple shear from mixing. This can bring new perspective to processes of precipitation and crystal growth[57] and may lead to methods of creating emulsions with novel microstructures. In the introduction we discussed efforts to use chaos to make polymer blends with designer morphologies. Metcalfe and Ottino[58] and Tang and Boozer[59] have shown computationally how the manifolds of chaotic transport can control yield and rate in some types of reacting flows; Ottino[60] has reviewed reactive flow chaotic advection. For dispersion of particles or fiber agglomerates our experiments show the elongationally dominated RAM flow to disperse nanoparticles into polymers to a much greater degree than conventional processing equipment.

A good mixer may also be a good heat exchanger, and heat exchange in highly viscous liquids is often problematic. Chagny et al.[44] have measured the enhancement of heat exchange brought about by a chaotic flow in a twisted pipe. Thermal homogenization for a chaotic duct flow can be estimated. For oils with Prandtl numbers greater than 20, and β_e and m taken from a globally chaotic RAM design solution, a RAM of 10–15 windows length would suffice to thermally homogenize highly viscous fluids.

Finally, in low *Re* microflows, while the particular method we have used to generate boundary motion would be a poor choice, the general idea of reorienting flow by surface generated fluid motion remains sound. Micro-RAM devices might use any surface actuation technique, for instance acoustic streaming or traveling flexural waves,[36] with the surface actuators added as layers in the fabrication process, while retaining tunable chaos at a microscale. As throughput demands increase and diffusion and reaction times are longer than device residence times, there will be a need for micromixers; moreover, chaotic flows could have multiple uses in microdevices.

We happily acknowledge a contribution by Shelley Erridge to the early part of this work, and we have benefited from discussions with Dr. Michel Speetjens, who also did the computation for Figure 17. Danny Stephenson gave additional technical and design support. Photographs and videos not taken by the authors were shot by Brooke Dunstan or Lawrence Cheung.

Power Scaling

To calculate rotational power input requirements for the RAM, first consider the work done on the fluid by a moving boundary element. Assuming for simplicity decoupling of the axial and in-plane flows, the power input at a window is the viscous shear stress at the window times the boundary velocity, integrated over the window area. Writing out the stress in cylindrical coordinates we have for the rotational power

$$P_r = \mu \Omega R^2 H \int_0^\Delta [r\partial_r(u_\theta/r) + r^{-1}\partial u_r] d\theta \qquad (8)$$

where u_θ, u_r are respectively the azimuthal and radial velocity components. The quantity inside the integral has units of shear rate, which we can either integrate numerically or for which we can estimate an upper bound by replacing the term in brackets with the maximum shear rate on the window boundary, which is Ω. The estimate being simpler, an upper bound on power input by a RAM window is

$$P_r \leq \mu H(\Omega R)^2 \Delta \tag{9}$$

For N windows, assuming no axial space between windows, we can replace H with L, the total length, to obtain for an entire RAM duct

$$P_r \leq \mu L(\Omega R)^2 \Delta \tag{10}$$

How sharp is this estimate? For a Newtonian fluid equation 10 overestimates P_r by about a factor of 10. We can see that from the inset of Figure 17, which plots the local shear rate. Higher shear rates are confined to the windows' azimuthal boundaries. From the graph in Figure 17 of the normalized frequency distribution of shear rate we see that the bulk of the flow, including along most of the window boundary, experiences a nearly constant shear that is $<\Omega/20$. Hence, equation 10 overestimates P_r by around an order of magnitude.

A similar calculation for the gap region (assuming it exists), assuming a Couette-type flow, gives the power dissipated in the gap. The estimate for the total required power input to the fluid is the sum of the power dissipated in the gap and Equation 10

$$P_r = \mu L(\Omega R)^2 \Delta \left[1 + \frac{2\pi - \Delta}{\Delta} \frac{R}{\delta} \right] \tag{11}$$

with δ the gap size. Depending on R/δ, dissipation in the small gap flow can be greater than Equation 10.

Due to the overestimate of Equation 10 and to the measurement ambiguity of exactly where energy is dissipated, it may be convenient to simplify P_r with an empirically determined dimensionless prefactor χ to obtain Eq. 5. Even though the required rotational power input for chaotic advection can be small, it may also be noted that the losses from the motor driving the rotation do *not* (in general) need to be dissipated in the fluid, which is important in some applications with a need to control the work input to the material during processing, perhaps to prevent heat damage.

In order to compare total power input P across devices on the same basis as we did with pressure drop, we want to scale P by P_{axt}, the axial pumping power required for an open tube

$$P = 1 + P_r/P_{axt} \tag{12}$$

From the discussion earlier $P_{axt} = \Delta P Q_v$ and, assuming a Poisieulle profile to calculate Q_v, combining Eqs. 5 and 12, while recalling the definition of β, we find Eq. 6.

These power comparisons may be extended a bit further. Power correlations for ribbon and anchor blenders are fashioned with products of power number and Reynolds number,[61] that is a power scaling of $\mu l^3 \Omega^2$, where l is a lengthscale and Ω is a rotation rate. In our terminology this is using P_r to scale Eq. 12 instead of P_{ax}. Applying this alternative scaling to Eq. 12, we obtain

$$P = \chi\Delta \left[1 + \frac{32\pi}{\chi\Delta} \left(\frac{\Gamma}{\beta} \right)^2 \right] \tag{13}$$

With the same assumptions for parameter values as above $P \approx 135$, which compares to values of 150–450 for ribbon and anchor blenders.[61] However, power is just one of many factors needed to fully compare batch and continuous blending.

Literature Cited

1. Hill M. Product and process design for structured products. *AIChE J.* 2004:50;1656–1661.
2. Ottino JM. *The Kinematics of Mixing: Stretching, Chaos and Transport.* Cambridge: U.K. Cambridge University Press; 1989.
3. Wiggins S. *Chaotic Transport in Dynamical Systems.* Springer-Verlag; 1992.
4. Aref H. The development of Chaotic Advection. *Phys Fluids* 2002: 14;1315–1325.
5. Metcalfe G, Rudman M. Fluid Mixer. patent US 2004/0013034 A1; 2004.
6. Horner M, Metcalfe G, Wiggins S, Ottino JM. Transport mechanisms in open cavities: effects of transient and periodic boundary flows. *J Fluid Mech.* 2002:452;199–229.
7. Biercuk MJ, Llaguno MC, Radosavljevic M, Hyun JK, Johnson AT, Fischer JE. Carbon nanotube composites for thermal management. *Appl Physics Lett.* 2002:80;2787–2789.
8. Todd DB. Mixing of Highly Viscous Fluids, Polymers, and Pastes. in *Handbook of Industrial Mixing: Science and Practice* Paul EL, Atiemo-Obeng VA, Kresta SM. eds. Wiley; 2004:987–1025.
9. McNeil B, Harvey LM. Viscous fermentation products. *Crit Rev in Biotech* 1993:13;275–304.
10. Elias CB, Joshi JB. Role of Hydrodynamic Shear on Activity and Structure of Proteins. in Scheper T. ed. *Advances in Biochemical Engineering/Biotechnology.* Springer, 1998:59;47–71.
11. Ottino J, Metcalfe G, Jana SC. Experimental Studies of Chaotic Mixing. in W. Ditto, L. Pecora, M. Shlesinger, M. Spano, and S. Vohra, eds. Proceedings of the 2nd Experimental Chaos Conference, Arlington, VA; World Scientific; 1995;3–20.
12. Kusch HA, Ottino JM. Experiments on mixing in continuous chaotic flows. *J Fluid Mech.* 1992:236;319–348.
13. Acharya N, Sen M. Heat transfer enhancement in coiled tubes by chaotic mixing. *Int J Heat Mass Transfer.* 1992:35;2475–2489.
14. Jana S, Tjahjadi M, Ottino JM. Chaotic mixing of viscous fluids by periodic changes in geometry—Baffled Cavity. *AIChE J.* 1994:40; 1769–1781.
15. Lamberto DF, Alvarez MM, Muzzio FJ. Experimental and computational investigation of the laminar flow structure in a stirred tank. *Chem Eng Sci.* 1999:54;919–941.
16. Fountain GO, Khakhar DV, Mezíc I, Ottino JM. Chaotic mixing in abounded three-dimensional flow. *J Fluid Mech.* 2000:417;265–301.
17. Zumbrunnen DA. Smart Blending: A Means to Obtain Fibers and Plastic Products with Tailored Properties. *J of Textile Inst.* 2000:91; 92–104.
18. Jana SC, Metcalfe G, Ottino JM. Experimental and computational studies of mixing in complex stokes flows: the Vortex mixing flow and multicellular cavity flows. *J Fluid Mech.* 1994:269;199–246.
19. Streiff FA, Jaffer S, Schneider G. The Design and application of static mixer technology. in proceedings ISMIP3, Osaka; 1999;107–114.
20. Arimond J, Erwin L. A Simulation of a Motionless Mixer. *Chem Eng Comm.* 1985:37;105–126.
21. Ling FM, Zhang XA. A Numerical study on mixing in the kenics static mixer. *Chem Eng Comm.* 1995:136;119–141.
22. Avalosse Th, Crochet MJ. Finite-element simulation of mixing: 1. Two-dimensional flow in periodic geometry. *AIChE J.* 1997:43;577–587.
23. Hobbs DM, Muzzio FJ. Optimization of a static mixer using dynamical systems techniques. *Chem Eng Sci.* 1998:18;3199–3213.
24. Liu S, Hrymak AN, Wood PE. Design Modifications to SMX Static Mixer for Improved Mixing, in proceedings of 19th annual meeting of Polymer Processing Society, Melbourne, 2003.
25. Avalosse TH, Crochet MJ. Finite-element simulation of mixing: 2. Three-dimensional flow through a kenics mixer. *AIChE J.* 1997:43; 588–597.
26. Bayer T, Pysall D, Wachsen O. Micro Mixing Effects in Continuous Radical Polymerization, in proceedings 6th World Congress of Chemical Engineering, Melbourne; 2001.

27. Kim S, Kwon T. Enhancement of mixing performance of single-screw extrusion processes via chaotic flows. *Adv Polym Tech.* 1996:15;41–54.
28. Jana SC, Scott E, Sundararaj U. Single extruder screw for efficient blending of miscible and immiscible polymeric materials. patent US 6132076; 1998.
29. Tjahjadi M, William FR. Single Screw Extruder Capable of Generating Chaotic Mixing. European patent EP 0 644 034 B1; 1999.
30. Kao SV, Mason SG. Dispersion of particles by shear. *Nature.* 1975: 253;619–622.
31. Sontag RC, Russell WB. Structure and breakup of flocs subjected to fluid stresses. *J Colloid and Interface Sci.* 1987:115;390–395.
32. Rauwendaal C, Oswald T, Gramann P, Davies B. Design of dispersive mixing devices. *Int Polym Proc.* 1999:13;28–34.
33. Zumbrunnen DA, Inamdar S, Kwon O, Verma P. Chaotic advection as a means to develop nanoscale structures in viscous melts. *Nano Lett.* 2002:2;1143–1148.
34. Sau M, Jana SC. A study on the effects of chaotic mixer design and operating conditions on morphology development in immiscible polymer systems. *Polymer Eng Sci.* 2004:44;407–422.
35. Jana SC, Sau M. Effects of viscosity ratio and composition on development of morphology in chaotic mixing of polymers. *Polymer.* 2004: 45;1665–1678.
36. Koch M, Evans A, Brunnschweiler A. *Microfluidic Technology and Applications.* Baldock: UK Research Studies Press; 2000.
37. Mensinger H, Richter Th, Hessel V, Döpper J, Ehrfeld W. Microreactor with Integrated Static Mixer and Analysis System, in van den Berg A and Bergveld P. eds. Micro Total Analysis Systems, Kluwer; 1995;237–243.
38. Liu RH, Stremler MA, Sharp KV, Olsen MG, Santiago JG, Adrian RJ, Aref H, Beebe DJ. Passive Mixing in a Three-Dimensional Serpentine Microchannel. *J of Microelectromechanical Systems.* 2000:9;190–197.
39. Tabeling P. Some Basic Problems of Microfluidics, in the proceedings 14th Australasian Fluid Mechanics Conference; Adelaide; 2001.
40. Oddy MH, Santiago JG, Mikkelsen JC. Electrokinetic Instability Micromixing. *Anal Chem.* 2001:73;5822–5832.
41. Stroock AD, Dertinger SKW, Ajdari A, Mezíc I, Stone HA, Whitesides GM. Chaotic mixer for microchannel. *Science.* 2002:295;647–651.
42. Wiggins S. Chaos in the dynamics generated by sequences of maps, with applications to chaotic advection in flows with aperiodic time dependence. *Zeitschrift für angewandte Mathematik und Physik.* 1999: 50;585–616.
43. Mezíc I. Chaotic advection in bounded navier-stokes flows. *J Fluid Mech.* 2001:431;347–370.
44. Chagny C, Castelain C, Peerhossaini H. Chaotic heat transfer for heat exchanger design and comparison with a regular regime for a large range of reynolds numbers. *App Thermal Eng.* 2000:20;1615–1648.
45. Hwu T-H, Young D-L, Chen Y-Y. Chaotic advections for stokes flows in circular cavity. *J Eng Mech.* 1997:August;774–782.
46. Renka RJ. SRFPACK: Software for scattered data fitting with a constrained surface under tension. *ACM Trans Math Soft.* 1996:22;9–17.
47. Jones SW, Thomas OM, Aref H. Chaotic advection by laminar-flow in a twisted pipe. *J Fluid Mech.* 1989:209;335–357.
48. Nauman EB, Buffham BA. *Mixing in Continuous Flow Systems.* John Wiley & Sons; 1983.
49. Raynal F, Gence J-N. Energy saving in chaotic laminar mixing. *Int J Heat Mass Transfer.* 1997:40;3267–3273.
50. Pahl M-H, Muschelknautz E. Static mixers and their applications. *Int Chem Eng.* 1982:22;197–205.
51. Byrde O. Massively Parallel Flow Computation with Application to Fluid Mixing. No 1736; École Polytechnique Fédérale de Lausanne; 1997, PhD thesis.
52. Byrde O, Sawley ML. Parallel computation and analysis of the flow in a static mixer. *Comput Fluids.* 1999:28;1–18.
53. Niederkorn TC, Ottino JM. Mixing of viscoelastic fluids in time-periodic flows. *J Fluid Mech.* 1993:256;243–268.
54. Niederkorn TC, Ottino JM. Mixing of shear thinning fluids in time-periodic flows. *AIChE J.* 1994:40;1782–1793.
55. Fan YR, Tanner RI, Phan-Thien N. A numerical study of viscoelastic effects in the chaotic mixing between eccentric cylinders. *J Fluid Mech.* 2000:412;197–225.
56. Fan YR, Phan-Thien N, Tanner RI. Tangential flow and advective mixing of viscoplastic fluids between eccentric cylinders. *J Fluid Mech.* 2001:431;65–89.
57. Ilievski D, Rudman M, Metcalfe G. The separate roles of shear rate and mixing on gibbsite precipitation. *Chem Eng Sci.* 2001:56;2521–2530.
58. Metcalfe G, Ottino JM. Autocatalytic processes in mixing flows. *Phys Rev Lett.* 1994:72;2875–2878.
59. Tang XZ, Boozer AH. Design criteria of a chemical reactor based on a chaotic flow. *Chaos.* 1999:9;183–194.
60. Ottino JM. Mixing and chemical reactions, a tutorial. *Chem Eng Sci.* 1994:49;4005–4027.
61. Saito S, Arai K, Takahashi K, Kuriyama M. Mixing and Agitation of Viscous FLuids. in *Encyclopedia of Fluid Mixing.* vol. 2. Cheremisinoff NP. ed. Gulf Publishing; 1986:901–948.

Manuscript received Dec. 16, 2004, and revision received May 13, 2005.